
This manuscript has been submitted for publication to the Geophysical Journal International. Please note that the manuscript has undergone 2 rounds of peer-review but has not yet been formally accepted for publication. Subsequent versions of this manuscript may have slightly different content. If accepted, the final version of this manuscript will be linked through this webpage. Please feel free to contact any of the authors; we welcome feedback.

The effect of lateral variations in Earth structure on Last Interglacial sea level

Jacqueline Austermann^{*1}, Mark J. Hoggard^{1,2,3}, Konstantin Latychev^{1,2}, Fred D. Richards⁴, & Jerry X. Mitrovica²

1. Lamont-Doherty Earth Observatory, Columbia University, New York, USA.
2. Department of Earth & Planetary Sciences, Harvard University, Cambridge, USA.
3. Research School of Earth Sciences, Australian National University, Canberra, Australia.
4. Department of Earth Science and Engineering, Imperial College London, London, UK

*jackya@ldeo.columbia.edu

Abstract

It is generally agreed that the Last Interglacial (LIG; ~130–115 ka) was a time when global average temperatures and global mean sea level were higher than they are today. However, the exact timing, magnitude, and spatial pattern of ice melt is much debated. One difficulty in extracting past global mean sea level from local observations is that their elevations need to be corrected for glacial isostatic adjustment (GIA), which requires knowledge of Earth's internal viscoelastic structure. While this structure is generally assumed to be radially symmetric, evidence from seismology, geodynamics, and mineral physics indicates that large lateral variations in viscosity exist within the mantle. In this study, we construct a new model of Earth's internal structure by converting shear wave speed into viscosity using parameterisations from mineral physics experiments and geodynamical constraints on Earth's thermal structure. We use this 3D Earth structure, which includes both variations in lithospheric thickness and lateral variations in viscosity, to calculate the first 3D GIA prediction for LIG sea level. We find that the difference between predictions with and without lateral Earth structure can be meters to 10s of meters in the near field of former ice sheets, and up to a few meters in their far field. We demonstrate how forebulge dynamics and continental levering are affected by laterally varying Earth structure, with a particular focus on those sites with prominent LIG sea level records. Results from four 3D GIA calculations show that accounting for lateral structure acts to increase local sea level by up to ~1.5 m at the Seychelles and minimally decrease it in Western Australia. We acknowledge that this result is only based on a few simulations, but if robust, this shift brings estimates of global mean sea level from these two sites into closer agreement with each other. We further demonstrate that simulations with a suitable radial viscosity profile can be used to locally approximate the 3D GIA result, but that these radial profiles cannot be found by simply averaging viscosity below the sea level indicator site.

Keywords:

Last Interglacial, Sea level, Glacial isostatic adjustment, Mantle viscosity

24 **1 Introduction**

25 The Last Interglacial (LIG; ~130–115 ka) is a time in Earth’s history during which global average temperatures
26 were 1–2°C warmer than pre-industrial values (Dutton *et al.*, 2015a). As such, it has been used as a testing
27 ground to study how ice sheets and sea level respond to past and possibly future warming (DeConto & Pollard,
28 2016; Fischer *et al.*, 2018). Reconstructions of global mean sea level (GMSL) during the LIG are based on
29 sea-level indicators, such as fossil corals, that constrain the local elevation of sea level at their time of formation
30 (Rovere *et al.*, 2016). Once locally reconstructed, this elevation has to be corrected for processes that cause a
31 deviation between local sea level and the GMSL. One of these processes is glacial isostatic adjustment (GIA),
32 which is the response of Earth’s solid surface, gravity field, and rotation axis to changes in ice and ocean mass.
33 GIA is an important contributor to interglacial sea-level change, even far away from major ice sheets (e.g.
34 Mitrovica & Milne, 2002; Lambeck *et al.*, 2012). In addition to GIA, other processes such as earthquakes,
35 crustal deformation, sediment loading, and dynamic topography can further deform Earth’s surface and cause
36 local sea-level change (Briggs *et al.*, 2014; Austermann *et al.*, 2017; Pico, 2019; Stephenson *et al.*, 2019).

37 Estimates of peak GMSL during the LIG, whether based on records from individual sites (Dutton *et al.*,
38 2015b; O’Leary *et al.*, 2013) or by combining data from multiple locations into a statistical framework (Kopp
39 *et al.*, 2009), are generally between 6–9 m. However, some recent work suggests that this range may be
40 overestimating GMSL during the LIG (Dyer *et al.*, in press.; Clark *et al.*, 2020). In general, significant debate
41 continues about both the magnitude of excess melt (relative to present day) and its timing: data from western
42 Australia indicate that GMSL exceeded present-day values by a few meters early in the LIG, followed by a
43 GMSL rise up to 9 m towards the end of the LIG (O’Leary *et al.*, 2013). This reconstruction is in disagreement
44 with estimates obtained from the Seychelles, which indicate that peak GMSL was attained early in the LIG and
45 continued to slowly increase, with possible intermittent sea level drops (Dutton *et al.*, 2015b; Vyverberg *et al.*,
46 2018; Hay *et al.*, 2014). While constraints from late LIG sea level are absent in the Seychelles, they are present
47 in Xcaret, Mexico – where sea level has been argued to undergo a step increase around 121 ka (Blanchon *et al.*,
48 2009) – and Mallorca, where speleothem records indicate constant or slightly falling GMSL throughout the LIG
49 (Polyak *et al.*, 2018). A global compilation of data indicates an oscillation in sea level with a highstand both
50 early and late (Kopp *et al.*, 2009), however this result is not strongly supported by either proximal ice records or
51 ice sheet dynamics (Barlow *et al.*, 2018).

52 Ongoing disagreement regarding the magnitude, timing, and spatial distribution of LIG melt raises the

53 possibility that complexities associated with the GIA correction may be responsible for some of these differences.
54 As noted above, each local sea-level estimate needs to be corrected for GIA to infer GMSL. The GIA correction
55 requires both an ice history and a viscoelastic structure for Earth's interior as input, both of which are under-
56 constrained. Uncertainties associated with the ice history can change the GIA correction by several meters
57 during the LIG (Dendy *et al.*, 2017; Rohling *et al.*, 2017; Lambeck *et al.*, 2012). In regard to Earth's viscoelastic
58 structure, previous studies of LIG sea level have all assumed that Earth's viscosity varies purely as a function of
59 depth. However, based on evidence from seismic tomography, mineral physics, and geodynamics, it is expected
60 that significant lateral variations exist in both Earth's viscosity and lithospheric structure (e.g. Dannberg *et al.*,
61 2017; Priestley *et al.*, 2018). Indeed, these lateral variations are important for understanding the impact of GIA
62 on sea level during the last deglaciation (Austermann *et al.*, 2013; Li *et al.*, 2018; Kuchar *et al.*, 2019) and affect
63 the pattern of present-day deformation across Antarctica (Nield *et al.*, 2018; Gomez *et al.*, 2018).

64 In this study, we focus on investigating how lateral variations in Earth structure affect sea level during the
65 LIG. We generate a new model of lateral Earth structure that is based on seismic tomography. In contrast to
66 previous work, which adopts a pre-determined scaling from shear wave speed into viscosity for the upper mantle
67 (Austermann *et al.*, 2013; Gomez *et al.*, 2018; Li *et al.*, 2018), we invert laboratory-based parameterisations for
68 material properties using a suite of independent constraints on mantle structure (Richards *et al.*, 2020). We pair
69 this Earth model with an ice history to predict the effect of lateral viscosity variations on sea level at key sites,
70 and provide physical insights into the GIA changes predicted both in the near and far field (i.e. close and distant
71 to the ice sheet). Given the computational expense of such calculations, we are limited to performing a relatively
72 small set of exploratory simulations, but these nevertheless provide a first estimate of the potential magnitude
73 and geometry of the LIG signal associated with realistic departures from radial mantle viscosity profiles. While
74 this work is focused on the LIG, insights on the physical mechanisms hold for any interglacial period and are
75 therefore also relevant to earlier interglacials (e.g., MIS 11) and the late Holocene. We also investigate how
76 well the GIA signal obtained when including lateral variability in Earth structure can, at a given location, be
77 accurately represented by a GIA model with a purely radial Earth structure. Lastly, we compare our results to
78 LIG sea level records at key sites to consider the extent to which lateral Earth structure and the associated GIA
79 prediction might impact estimates of GMSL over the LIG.

80 **2 Methods and Data**

81 **2.1 GIA numerical model**

82 To investigate how GIA causes spatially varying sea level over the LIG, we use a finite volume-based approach
83 to solve for radial displacement of the solid Earth, its change in gravity field, and rotation axis in response to
84 an evolving ice and ocean load (Latychev *et al.*, 2005). The numerical approach incorporates lateral variations
85 in Earth structure and calculates the resulting, gravitationally self-consistent sea-level change, while accurately
86 accounting for shoreline migration Mitrovica & Milne (2003). This computational model is well established,
87 having been used in many previous studies (e.g. Austermann *et al.*, 2013; Kuchar *et al.*, 2019; Gomez *et al.*, 2018;
88 Goldberg *et al.*, 2016). GIA calculations described here for radially symmetric Earth structure are performed
89 using both the finite volume approach described above and the pseudo-spectral approach described in Kendall
90 *et al.* (2005).

91 **2.2 Ice reconstruction**

92 The ice reconstruction we adopt is based on a combination of several published studies in order to obtain
93 satisfactory fits to multiple independent datasets (Fig. 1). From the present-day back to 26 ka, we use the
94 deglacial ice sheet reconstruction ICE-6G (Peltier *et al.*, 2015). For the preceding glaciation, we use the
95 reconstructions by Pico *et al.* (2017) and Creveling *et al.* (2017), which are more consistent with sea-level
96 observations from these time periods. To isolate the GIA contribution to sea level during the LIG, we assume
97 present-day ice geometry from 128–117 ka. Any excess ice melt beyond the present-day level will, of course,
98 produce an additional geographically varying sea-level fingerprint, which introduces additional uncertainty
99 (Hay *et al.*, 2014). The timing and melt geometry of the penultimate deglaciation has been widely debated,
100 with estimates including a much smaller (Rohling *et al.*, 2017) or larger (Shakun *et al.*, 2015) overall ice
101 volume compared to the last deglaciation; a deglaciation that commenced early (around 140 ka; Thomas *et al.*,
102 2009) or late (closer to 135 ka; Waelbroeck *et al.*, 2002); and an ice distribution characterised by a slightly
103 (Lambeck *et al.*, 2006) or significantly (Colleoni *et al.*, 2016) larger Fennoscandian ice sheet relative to LGM.
104 The ice geometry and timing of melt across the penultimate deglaciation will significantly affect GIA during
105 the LIG and has been explored in detail elsewhere (Dendy *et al.*, 2017; Rohling *et al.*, 2017). Here, we adopt a
106 representative ice history that has an ice volume at the penultimate glacial maximum (PGM) that is similar to
107 the last glacial maximum (LGM; consistent with oxygen isotope estimates; Waelbroeck *et al.*, 2002), a slightly

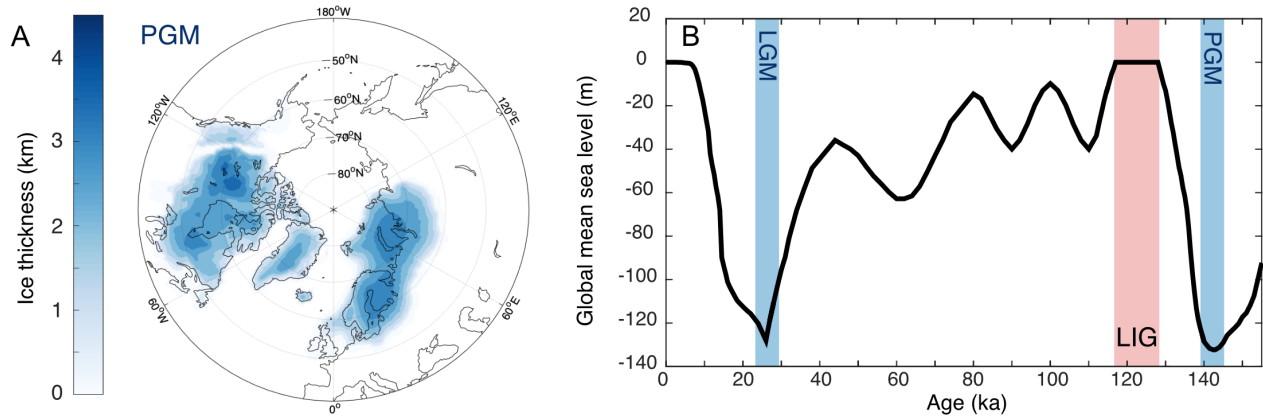


Figure 1: **Ice model reconstruction.** A) Distribution of northern hemisphere ice during the penultimate glacial maximum (PGM) used in our model. The Fennoscandian ice sheet is based on Lambeck *et al.* (2006). B) Global mean sea level with respect to present day over the course of the model. Vertical coloured bars indicate timings of the last glacial maximum (LGM), Last Interglacial (LIG), and penultimate glacial maximum.

108 slower deglaciation than during the last deglaciation (in line with U–Th dated corals from Tahiti; Thomas *et al.*,
 109 2009), and an ice distribution characterised by a larger Fennoscandian ice sheet, following Lambeck *et al.*
 110 (2006), and in turn smaller Laurentide ice sheet (Fig. 1). Our calculations start at 150 ka and continue until the
 111 present day.

112 2.3 Elastic Earth structure

113 To model the instantaneous elastic deformation of the solid Earth in response to evolving ice loads, we require
 114 estimates of the bulk and shear moduli of the mantle. We adopt the radially symmetric model STW105
 115 (Kustowski *et al.*, 2008), which uses more data and an improved inversion scheme and crustal correction
 116 compared to earlier studies such as PREM (Dziewonski & Anderson, 1981). We emphasise that the choice of
 117 the elastic structure has only a minimal effect on our results (i.e. on the order of centimetres during the LIG).
 118 While elastic moduli are known to vary laterally, these perturbations are considerably smaller than those in
 119 viscosity and do not play a first-order role in the GIA response. We therefore maintain a radially symmetric
 120 elastic structure and only investigate the effect of lateral viscosity variations in this study.

121 2.4 Viscous Earth structure including lithospheric thickness variations

122 The mantle convects with a time-dependent planform that evolves on million-year timescales and introduces
 123 significant lateral temperature heterogeneity (Turcotte & Schubert, 2002). Laboratory experiments on the

124 deformation of mantle rocks show that their viscosity is strongly dependent on temperature, and it has therefore
125 long been known that significant lateral variations in viscosity occur within the mantle (Cathles, 1975; Ranalli,
126 1995). The velocity of seismic waves is also sensitive to mantle temperature and rheology, and seismic
127 tomography is our most direct tool for imaging mantle structure (Bullen, 1975).

128 Seismic velocities are traditionally converted into temperature and then viscosity using a combination of
129 physical and phenomenological laws (e.g. thermal expansion, an Arrhenius relationship to describe the tem-
130 perature dependence of viscosity) and material properties that have been derived from laboratory experiments.
131 Here, we construct a mantle viscosity structure that relies on these same conversion relationships, including
132 an up-to-date treatment of anelasticity at seismic frequencies that is detailed below. As with previous studies,
133 uncertainties in the appropriate material properties, the rheological deformation mechanism responsible for
134 accommodating GIA motions, and variations in measured seismic velocity structure between different tomogra-
135 phy models all introduce uncertainty into the resulting viscosity structure. In contrast to other studies, however,
136 we leverage additional information on the thermal and rheological state of the upper mantle to optimise the
137 selection of appropriate material properties. This approach substantially reduces uncertainties in inferred mantle
138 viscosity structure, which is demonstrated and discussed in Section 4.1.

139 **2.4.1 Viscosity above the transition zone and lithospheric thickness**

140 When a polycrystalline viscoelastic material such as the mantle is cold, deformation associated with the passage
141 of acoustic energy is elastic, yielding a linear dependence of V_S on temperature referred to as the *anharmonic ve-*
142 *locity*. As temperature increases, however, *anelastic* deformation (a special case of fully recoverable viscoelastic
143 deformation) also begins to occur due to the presence of point defects, dislocations, and grain boundaries. This
144 additional process results in a non-linear relationship between V_S and temperature and is particularly important
145 to account for when inferring viscosity in high-temperature regions (Karato, 1993; Wu *et al.*, 2012). Anelastic
146 behaviour has been extensively studied in laboratory experiments on silicates and organic analogues of mantle
147 rocks, revealing that the strength of the anelastic regime varies with both the frequency of seismic waves and
148 as a function of material properties, such as melting temperature and grain size (Sundberg & Cooper, 2010;
149 McCarthy *et al.*, 2011; Faul & Jackson, 2015). Several studies have attempted to parameterise these complex
150 dependencies and have been regularly updated as forced oscillation and creep experiments in the laboratory
151 have been pushed towards increasingly realistic frequencies, pressures, temperatures, grain sizes, and strain
152 rates (Jackson & Faul, 2010; Takei, 2017).

153 In this study, we map shear-wave velocity (V_S) into temperature and viscosity in the upper 400 km of
154 the mantle using the parameterisation of Yamauchi & Takei (2016), which has been developed through forced
155 oscillation experiments on borneol. The parameterisation accounts for the effects of anelasticity in pre-melt
156 conditions, when temperature (T) exceeds $\sim 90\%$ of the melting temperature (T_m ; both defined in Kelvin).
157 These conditions most often occur in regions of the asthenosphere that underlie thin lithosphere, such as beneath
158 West Antarctica, which is a site that experiences significant ice mass changes over the glacial cycle. Specific
159 details on the representation of anelasticity are provided in Appendix A. To summarise, seismic velocity and
160 attenuation are self-consistently tied to temperature and steady-state diffusion creep viscosity via a system
161 of coupled equations that depend on seven material properties (including the activation energy, E_a , which
162 controls the dependence of viscosity on temperature through an Arrhenius relationship). Here, we assume that
163 temperature is the dominant cause of seismic velocity variations and that grain size and composition play only a
164 second-order role. The equations that are being used in this study are given by Equations (3)–(17) of Richards
165 *et al.* (2020).

166 The standard approach is to adopt material properties and their associated uncertainties that are appropriate
167 for upper mantle rocks (typically olivine) and have been obtained from laboratory experiments (e.g. Kaufmann
168 *et al.*, 2005; van der Wal *et al.*, 2010; Li *et al.*, 2018). Here, rather than fixing these properties using an
169 assumed mineralogy, we take advantage of an inverse calibration scheme outlined in Richards *et al.* (2020)
170 that considerably reduces uncertainty in inferred mantle structure (see Section 4.1). The philosophy behind the
171 approach is that certain physical properties of the Earth are ‘known’, including the typical thermal structure
172 of oceanic lithosphere, the average adiabatic temperature profile within the convecting mantle, the attenuation
173 structure of the upper mantle beneath old oceanic lithosphere, and the mean diffusion creep viscosity of the
174 upper mantle from studies of GIA. Any model of upper mantle temperature and viscosity structure inferred
175 from shear wave velocities should be compatible with these constraints, and we therefore restrict ourselves to a
176 subset of material properties that also satisfy these physical characteristics.

177 To generate the constraints, we first stack shear-wave velocities from the tomography model as a function
178 of depth and oceanic age. Temperature contours from the Richards *et al.* (2018) plate cooling model are
179 subsequently overlain and V_S - T tie points at depths of 75 km, 100 km, and 125 km are extracted. A second
180 set of deeper tie points is generated by assuming that the average value of V_S as a function of depth over the
181 225–400 km range should yield a temperature that is consistent with the 1333°C adiabat. A third constraint is
182 obtained by overlaying the observed attenuation structure at depths of 150–400 km beneath > 100 Ma seafloor

183 from the QRFS112 model of Dalton *et al.* (2009) on the equivalent V_S stack, in order to generate a set of V_S - Q^{-1}
 184 tie points as a function of depth. Finally, we require that the mean diffusion creep viscosity from 225–400 km
 185 depth be equivalent to the average upper mantle value of 3×10^{20} Pa s that has been obtained from previous
 186 studies of GIA (Lau *et al.*, 2016). We calculate a range of predicted temperature, attenuation, and viscosity maps
 187 by varying the seven material properties and comparing the results to the calibration targets described above.
 188 Misfit is optimised by iteratively updating the material properties. To reduce the likelihood of locating local
 189 minima in the inversion, we use a two-step minimisation algorithm consisting of an initial, relatively coarse
 190 parameter sweep followed by Powell’s conjugate gradient algorithm. Further details on this calibration scheme
 191 can be found in Richards *et al.* (2020).

192 Here, we use the SL2013sv tomography model, which has global coverage in the upper mantle, and patch in
 193 the SL2013NA regional update in North America that takes advantage of the dense station coverage afforded by
 194 the USArray seismic network (Schaeffer & Lebedev, 2013, 2014). We have chosen this model for two reasons.
 195 First, it has high horizontal resolution (~ 280 km horizontal node spacing) and is constructed from both body
 196 waves and a large quantity of surface wave data (including higher modes), which are particularly sensitive
 197 to velocity structure in the upper ~ 350 km of the mantle. Secondly, density and temperature fields derived
 198 from this model have been shown to correlate well with independent geophysical and geological observations
 199 including gravity anomalies, residual topography, continental geotherms, and mineral deposits (Steinberger,
 200 2016; Hoggard *et al.*, 2017, 2020). The anelastic calibration scheme yields optimal material properties of
 201 74.7 GPa for the reference shear modulus (with 1σ uncertainties of approximately 3%). Its dependence on
 202 temperature is -16.1 MPa $^{\circ}\text{C}^{-1}$ ($\sim 12\%$) and on pressure is 2.56 (dimensionless, $\sim 7\%$), respectively. The
 203 reference diffusion creep viscosity is 2.51×10^{21} Pa s ($\sim 8\%$), and its dependence on temperature and pressure
 204 are controlled by an activation energy of 304 kJ mol^{-1} (± 250 kJ mol^{-1}) and activation volume of 3.0 cm^3 mol^{-1}
 205 (± 6.0 cm^3 mol^{-1} , uncertainties are again 1σ). We note that a negative activation volume implies that the
 206 sensitivity of viscosity to temperature may decrease with depth, which has been previously suggested for mantle
 207 mineral assemblages when self-diffusion of certain ions (such as Si and O) becomes rate-limiting (Fei *et al.*,
 208 2018; Jain *et al.*, 2019). The solidus gradient is 0.946 $^{\circ}\text{C km}^{-1}$ ($\sim 25\%$). The resulting scaling relationship
 209 between shear wave velocity and lateral viscosity perturbations is shown in Fig. 2. Throughout the manuscript
 210 we define lateral viscosity perturbations as $\log_{10} \frac{\eta_1}{\eta_0}$. The effect of accounting for anelastic effects in this manner
 211 is to increase viscosities by between 1 and 1.5 orders of magnitude in the slowest V_S , lowest-viscosity locations,
 212 in comparison to a purely anharmonic conversion (Fig. 2 E). Viscosities are unaffected in faster velocity regions

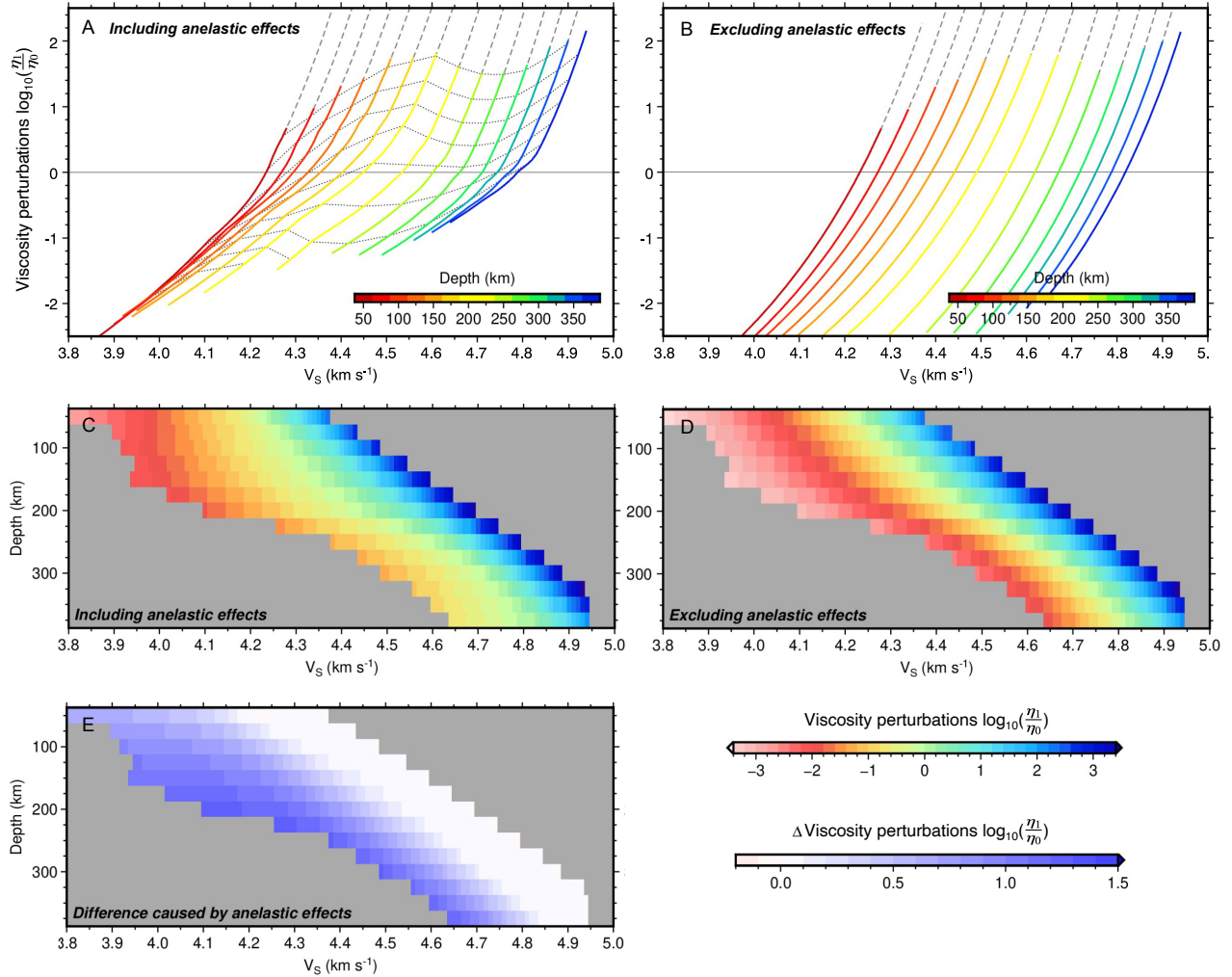


Figure 2: Conversion of shear wave speed to viscosity perturbations. A) Calibrated relationship between shear wave velocity (V_S) and the logarithm of lateral viscosity perturbations as a function of depth for our calibrated upper-mantle model of anelasticity at seismic frequencies (Schaeffer & Lebedev, 2013, 2014; Yamauchi & Takei, 2016; Richards *et al.*, 2020). Coloured lines transition to dashed grey at the lithosphere-asthenosphere boundary (i.e. 1175°C); black dotted lines = isothermal contours from 1200°C to 1600°C at 50°C increments. B) Same if anelastic effects are excluded. C, D) Same values as in A and B, respectively, but plotted as V_S versus depth and coloured by viscosity perturbations. E) Difference between C and D, illustrating that including anelastic effects primarily acts to increase the inferred viscosity at slow shear wave velocities. Throughout this study, we include anelastic effects and use the conversion shown in panels A and C.

213 where temperatures are colder (i.e. $T < 0.9T_m$).

214 Lithospheric thickness is identified using the depth of the 1175°C isothermal surface, which has an average
 215 global value of ~ 100 km and varies from ~ 300 km in cratonic regions to < 25 km in sites of active rifting and
 216 at mid-oceanic spreading centres (Fig. 3A, Hoggard *et al.*, 2020). This specific isotherm is chosen because it

217 coincides with seismological evidence for the depth of the lithosphere-asthenosphere boundary in oceanic regions
218 (Richards *et al.*, 2018). At 100 km depth, a temperature of 1175°C corresponds to a diffusion creep viscosity of
219 4.5×10^{22} Pa s in our anelasticity parameterisation, which yields a characteristic Maxwell time of ~ 20 kyr. We
220 therefore consider this boundary an adequate representation of the transition between asthenospheric material
221 that undergoes viscoelastic deformation during the simulation, and lithospheric material that only deforms
222 elastically. It has been suggested that lithospheric thickness on GIA timescales likely appears thinner than
223 inferred over the seismic cycle due to the onset of viscous or transient deformation (Watts *et al.*, 2013; Lau *et al.*,
224 2020). We therefore perform an additional sensitivity test where lithospheric thickness is reduced everywhere
225 by 20% (i.e., 80 km global average).

226 **2.4.2 Viscosity within and beneath the transition zone**

227 Deeper than 400 km, the sensitivity of surface waves to velocity structure drops significantly, the dominant
228 mantle mineralogy switches from olivine to wadsleyite, and the number of independent constraints on mantle
229 properties is considerably more limited. For these reasons, we use a different approach to estimate viscosity
230 perturbations below 400 km depths and linearly blend the upper and lower viscosity model over the 300-400 km
231 depth range. For the tomography model, we take the whole mantle SEMUCB-WM1 model, which is constructed
232 using a combination of body and surface wave data and uses a sophisticated hybrid approach to numerically
233 simulate wavefield propagation and invert waveforms for shear wave-velocity structure (French & Romanowicz,
234 2014).

235 To generate lower mantle viscosity perturbations, we first convert V_S into temperature using the `Perple_X`
236 Gibbs free-energy minimisation software of Connolly (2005) and the thermodynamic database of Stixrude
237 & Lithgow-Bertelloni (2011). Assuming a pyrolitic composition, the mineralogical make-up is estimated as a
238 function of pressure and temperature, yielding predictions of the elastic moduli and density that can be converted
239 into anharmonic velocity. At a given depth and for an individual mineral assemblage, these material properties
240 exhibit an approximately linear dependence on temperature, resulting in a unique conversion from anharmonic
241 velocity into temperature. In the vicinity of phase transitions, however, a discontinuity occurs that can render
242 this conversion non-unique. To avoid this issue, at each depth, we first linearise the temperature-dependence
243 of the density and elastic moduli over a temperature window that extends $\pm 500^\circ\text{C}$ around a quasi-steady state
244 geotherm obtained from mantle convection simulations (Supplementary Material; Schubert & Bunge, 2009).
245 The anharmonic velocity as a function of pressure and temperature is subsequently corrected for anelastic effects

246 using the Q5 radial attenuation profile and equations 1 & 2 of Cammarano *et al.* (2003) and a mantle solidus from
247 Andraut *et al.* (2011). To ensure that we obtain a self-consistent mantle geotherm from the tomography model,
248 we extract the V_S variation over the $\pm 500^\circ\text{C}$ temperature window and pin the absolute V_S at the geotherm
249 temperature to the average V_S of the tomography model at this depth. Thus lateral V_S variations at any depth
250 are mapped into temperature variations around the average geotherm. Finally, these temperature variations
251 are converted into viscosity perturbations using a radial activation enthalpy profile constructed from our upper
252 mantle result extended down to 660 km, followed by the lower mantle profile of Steinberger & Calderwood
253 (2006).

254 **2.4.3 Resulting viscosity structure**

255 Our resulting lithospheric thickness and viscosity perturbations at specific depths are shown in Fig. 3 and are
256 provided as supplementary material. As expected, thick lithosphere aligns with cratonic regions and it thins
257 towards mid-ocean ridges. Oceans are generally underlain by a less viscous asthenosphere and higher viscosity
258 slabs appear beneath subduction zones at greater depth. The general patterns and order of magnitude viscosity
259 variations are comparable to previously derived viscosity structures (Li *et al.*, 2018). For our GIA calculations,
260 we superimpose the lateral viscosity perturbations shown in Fig. 3 on different 1D viscosity profiles. Our
261 default simulations use a 1D viscosity profile referred to as p55, which consists of an upper mantle viscosity of
262 5×10^{20} Pa s and a lower mantle viscosity of 5×10^{21} Pa s (Raymo *et al.*, 2011). Uncertainties in inferred Earth
263 structure and their impacts on GIA predictions are discussed in Section 4.1.

264 **3 Results**

265 We performed GIA calculations using both radially symmetric and laterally varying viscosity structure, which
266 we will refer to as 1D and 3D simulations, respectively. Results and predictions from these simulations will be
267 referred to as 1D and 3D results and predictions. The 1D viscosity model is identical to the average of the 3D
268 viscosity model (averaging is done in log space) at each depth except in the analysis described in section 4.3.
269 We first describe and explain the general patterns that are common to both 1D and 3D simulations. We next
270 detail differences between 1D and 3D results in the near and far field, before comparing results at specific sites
271 with important sea-level indicators from the LIG.

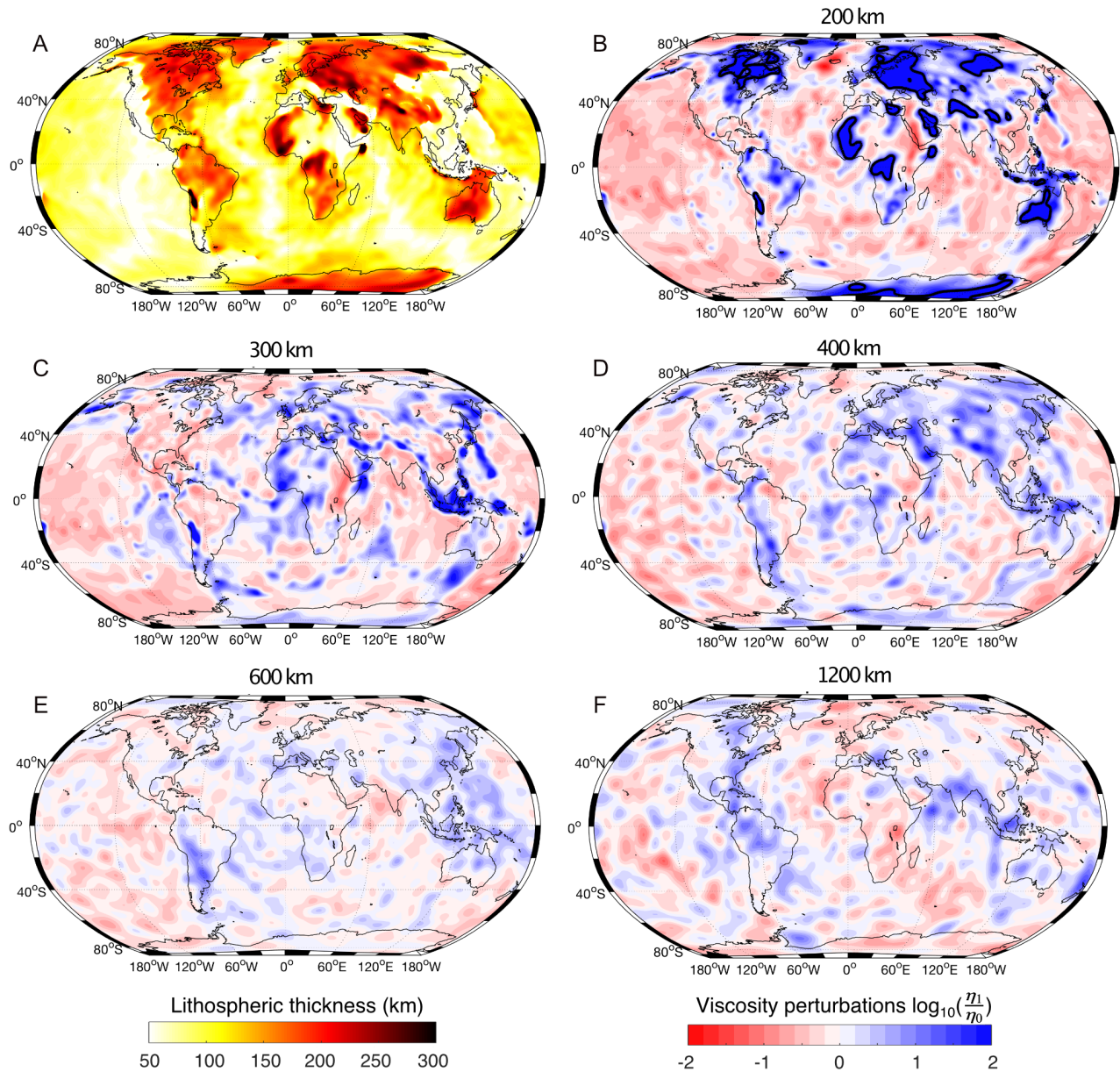


Figure 3: **3D viscosity structure of the Earth.** A) Global lithospheric thickness variations, yielding a globally averaged lithospheric thickness of 100 km (colorbar at the bottom left). B–F) \log_{10} of the lateral viscosity perturbations at depths of 200 km, 300 km, 400 km, 600 km, and 1200 km, respectively (colorbar at the bottom right). Thick black contour in panel (B) delineates lithospheric portions.

272 **3.1 General patterns of GIA over the LIG**

273 **Near field.** GIA models predict that sea level changes over the course of an interglacial will vary significantly
274 across the globe (Raymo & Mitrovica, 2012; Dutton & Lambeck, 2012; Dendy *et al.*, 2017). At the beginning
275 of the LIG (Fig. 4A), relative sea level (i.e., sea level relative to present-day; Mitrovica & Milne, 2003) is high
276 in formerly glaciated regions because these areas are experiencing ongoing postglacial rebound in response to
277 the just-completed deglaciation, while the peripheral bulges surrounding them are subsiding from an elevated
278 position, leading to low values of relative sea level. That is, the solid Earth beneath the major ice sheets is in
279 greater isostatic disequilibrium at the beginning of the LIG compared to today. For the Laurentide ice sheet,
280 this pattern is reversed at the end of the LIG (Fig. 4B) at which time more rebound (and peripheral bulge
281 subsidence) has occurred in comparison to today. This is the case because the LIG was longer than the present
282 interglacial and because our ice history adopts a Laurentide ice sheet that was smaller during the PGM than
283 the LGM. In contrast, the results for the Fennoscandian region suggest more isostatic disequilibrium at the end
284 of the LIG compared to today (Fig. 4B) – the formerly glaciated area remains below present levels while the
285 peripheral bulge sits above present levels. In this case, the greater size of the Fennoscandian ice sheet at PGM
286 relative to the LGM more than compensates for the fact that the duration of the LIG was longer than the duration
287 of the present interglacial.

288 **Far field.** First-order sea-level patterns in the far field include continental levering, ocean syphoning,
289 and rotational effects (Mitrovica & Milne, 2002). Continental levering – a tilting of the crust at continental
290 shorelines – is driven by the loading and unloading of the oceans by the water produced from ice melting, while
291 the adjacent continents experience no such load changes. During interglacials, the process leads to a progressive
292 rise in sea level on the oceanward side of a continental shoreline and a fall on the continent side of the shoreline.
293 The length scale of this effect is related to the thickness of the lithosphere, with thicker lithosphere leading to a
294 broader levering signal that extends further away from the shoreline. The levering process is significantly more
295 advanced at present-day relative to the start of the LIG, leading to the strong gradient in sea level on a transect
296 across most shorelines (Fig. 4A). In contrast, at the end of the LIG, the levering process is somewhat more
297 advanced than at present day, and the gradient along the transect is therefore of opposite sign and smaller in
298 magnitude (Fig. 4B). In the middle of ocean basins, ocean-syphoning – the migration of water away from such
299 regions and largely toward subsiding peripheral bulges – dominates sea-level physics during interglacials and
300 drives a sea-level fall. At the beginning of the LIG, this process is less advanced than at present day and sea
301 level is higher than at present (Fig. 4A), while at the end of the (longer duration) LIG, the opposite is true and

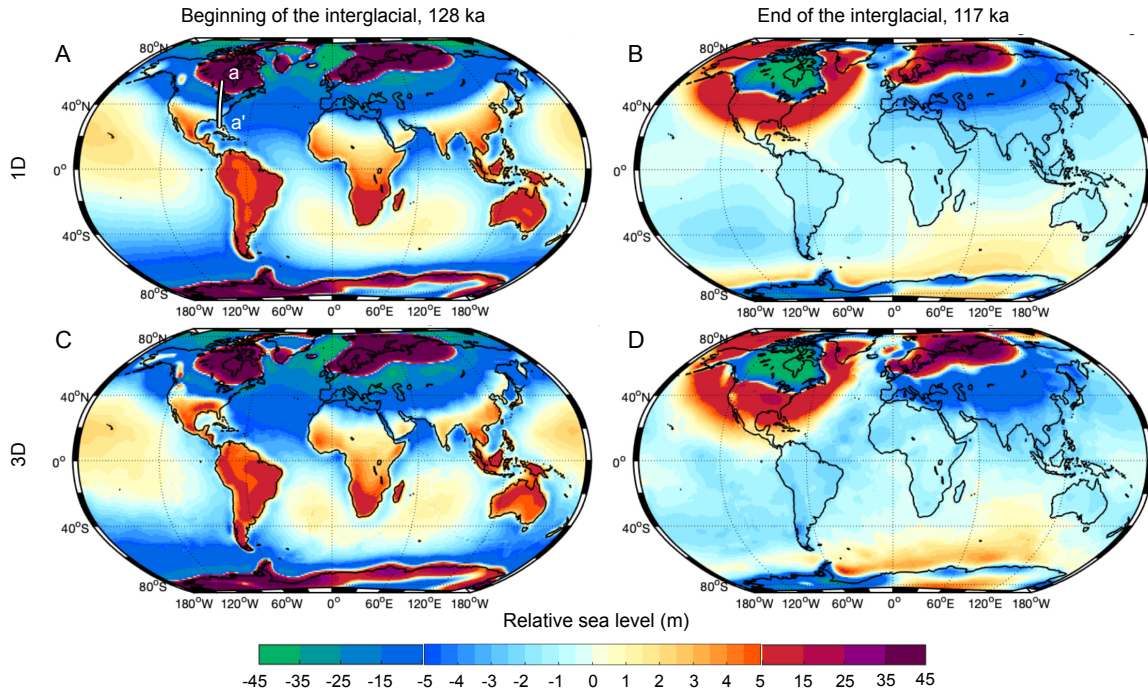


Figure 4: **LIG sea level predictions assuming 1D and 3D Earth structure.** A, B) Prediction of relative sea level at the beginning (128 ka) and end (117 ka) of the Last Interglacial, respectively, assuming radially symmetric Earth structure. C, D) Same as A, B but including lateral variations in lithospheric thickness and mantle viscosity. The a–a’ transect indicated in panel A is used in Fig. 6.

302 sea level is lower (Fig. 4B).

303 Models that include lateral variability in Earth structure exhibit the same first-order patterns described above
 304 (Fig. 4C, D). However, there are notable shorter wavelength differences that arise due to lateral variations in
 305 both lithospheric structure (Fig. 5A, B), and mantle viscosity (Fig. 5C, D). The magnitude of the difference
 306 between 1D and 3D predictions is largest in the near field, where it is on the order of several to tens of meters.
 307 The difference is smaller, but still up to few meters, in the far field of ice sheets (Fig. 5E, F). In the next section,
 308 we analyse in more detail the differing GIA responses.

309 **3.2 Near-field effects of lateral variations in Earth structure**

310 **Lithospheric thickness variations alone.** Both regions that were covered by massive ice sheets during the
 311 PGM, Fennoscandia and Canada, are largely cratonic regions with a thick continental lithosphere (Fig. 3A).
 312 This similarity leads to similar patterns in North America and northern Europe when comparing the 1D and 3D
 313 results (Fig. 5A). The thicker lithosphere underneath the former Laurentide ice sheet leads to less subsidence

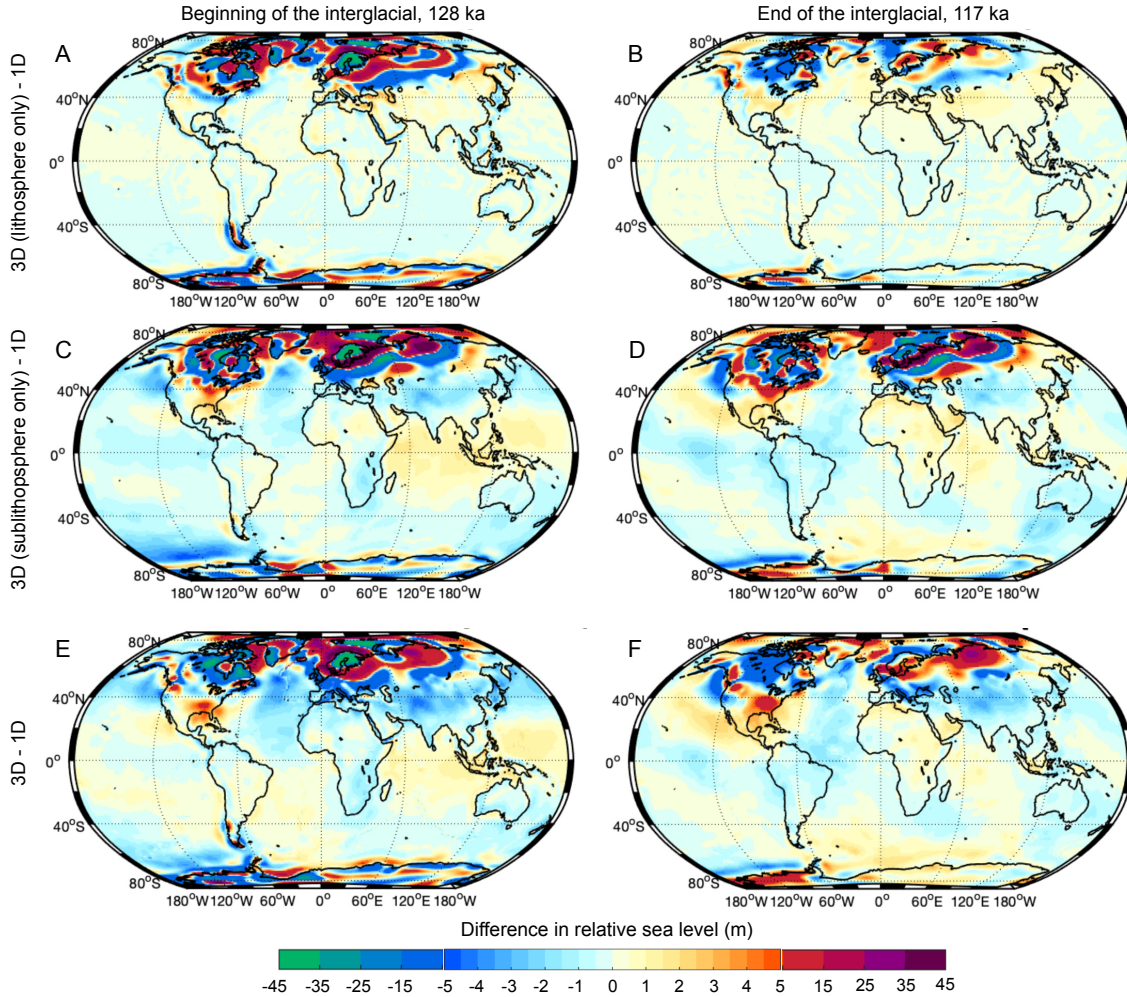


Figure 5: **Effect of lateral variations in Earth structure on LIG sea level.** A, B) Difference in predicted sea level at the beginning (128 ka) and end (117 ka) of the Last Interglacial, respectively, between a simulation with variable lithospheric thickness above a radial viscosity profile and one with constant lithospheric thickness. C, D) Difference in predicted sea level at the beginning (128 ka) and end (117 ka) of the Last Interglacial, respectively, between a simulation with variable sublithospheric viscosity variations and one with radially symmetric viscosity (both simulations have a constant lithospheric thickness). E, F) Difference in predicted sea level at the beginning (128 ka) and end (117 ka) of the Last Interglacial, respectively, between a simulation including lateral variations in both lithospheric thickness and viscosity, and a purely radial model.

314 and a more distal peripheral bulge during the glacial maxima. At the beginning of the LIG, when ice sheets were
315 recently melted, this leads to higher topography (or lower sea level) in the centre of the former ice sheet with a
316 broader peripheral bulge (Fig. 5A; Fig. 6A). Towards the end of the LIG, as the peripheral bulge continues to
317 subside, the difference between the 1D and 3D results is small (Fig. 5B; Fig. 6B). Sea level in Fennoscandia
318 exhibits a similar pattern at the beginning of the LIG except in western Europe (UK, Germany, France), which
319 can be explained by the much thinner lithosphere in this region (Fig. 3A). The predicted response evolves
320 towards the end of the LIG as the centre of rebound shifts slightly northwards (Fig. 5B).

321 **Lateral variability in both lithospheric thickness and mantle viscosity.** We next consider the effects of
322 including lateral variations in mantle viscosity in addition to lithospheric thickness variations. In Fennoscandia,
323 the patterns change only slightly, most notably in western Europe (UK, Germany, France). These areas have a
324 thin lithosphere but are underlain by mantle at 300–400 km depth that is 1–2 orders of magnitude more viscous
325 than the global average. This high-viscosity feature, which is a slab associated with the closure of the Tethys
326 Ocean (specifically the Apennine–Calabrian–Maghrebides slab; Fichtner *et al.*, 2013; van Hinsbergen *et al.*,
327 2014), causes a widening of the peripheral bulge observed in the 3D - 1D difference, both at the beginning and
328 end of the LIG (Fig. 5 C-F). Considering the peripheral bulge of the Laurentide ice sheet along the US East
329 coast, we find that lateral viscosity variations bring the location of the bulge closer to the former ice sheet (Fig.
330 5 C, D) while remaining similar in amplitude (Fig. 6A). A significant difference between the 3D simulation
331 and the 1D result is visible at the southern end of the peripheral bulge (i.e. south of $\sim 37^\circ\text{N}$), which is underlain
332 by low viscosity mantle at ~ 300 km depth (Fig. 6E). This weak region has previously been associated with
333 active upwelling flow above the Farallon slab (Rowley *et al.*, 2013). We speculate that the low viscosity in this
334 region focuses deformation associated with the peripheral bulge and possibly also continental levering, leading
335 to a relative sea-level high and more northern peripheral bulge in comparison to runs that only account for
336 lithospheric thickness variations (Fig. 6). This leads to a relative sea-level high that persists throughout the
337 deglaciation and LIG (Fig. 4C-F; Fig. 6A-D). This response is also visible along the US west coast, which is
338 generally underlain by lower viscosity mantle. It is, however, more localised at the edge of the former ice sheet,
339 with a sea-level peak occurring around 47°N .

340 **3.3 Far-field effects of lateral variations in Earth structure**

341 **Lithospheric thickness variations alone.** Many far-field sea-level sites are located at continental margins that
342 sit on the transition from thinner oceanic lithosphere to thicker continental lithosphere (Fig. 3B). This differs

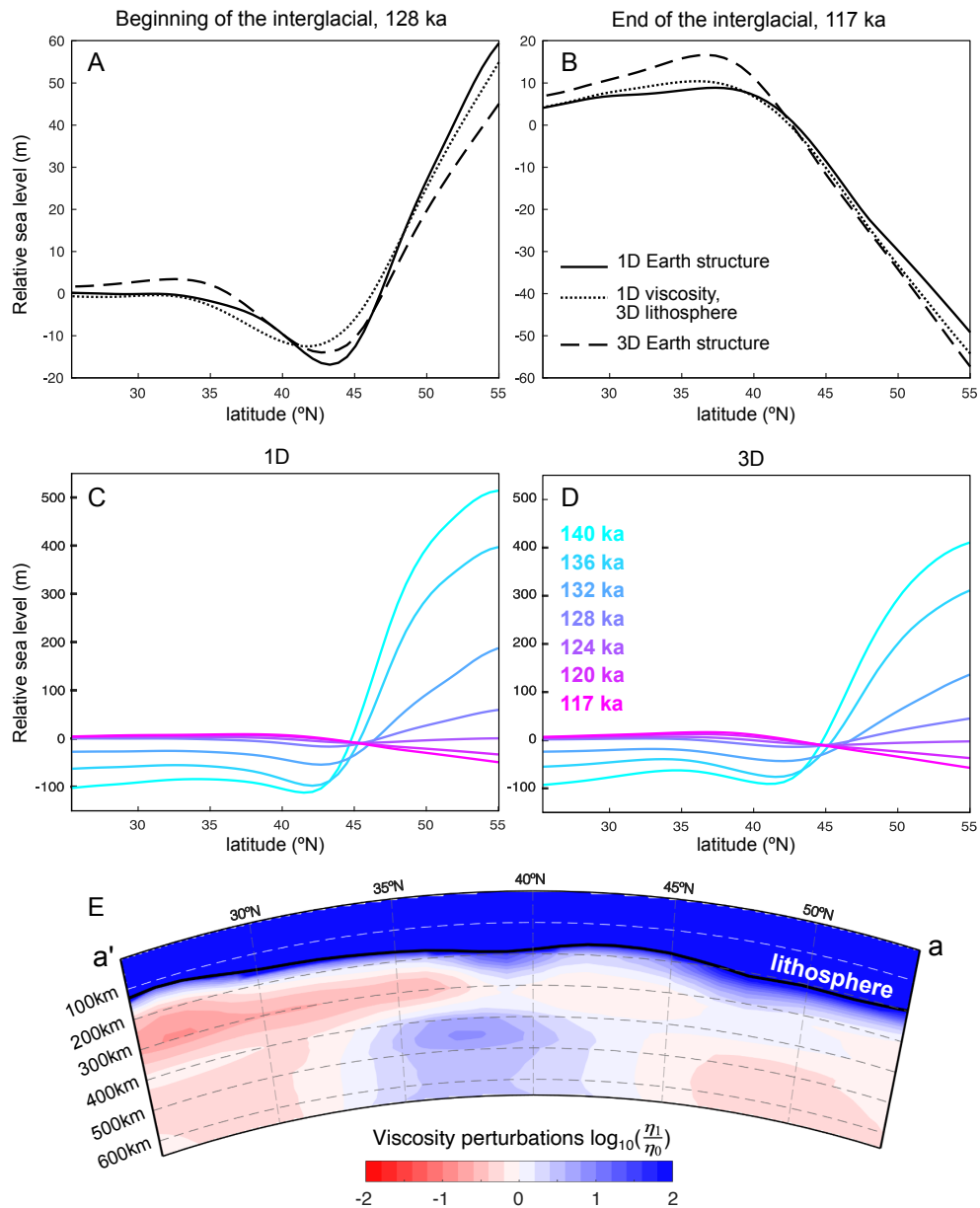


Figure 6: **Near-field GIA effects due to lateral variations in Earth structure.** A, B) Relative sea level at the beginning (128 ka) and end (117 ka) of the LIG across the peripheral bulge of the Laurentide ice sheet (a–a’ transect of Fig. 4A). Results are shown for simulations using a 1D Earth structure (black line) with a constant lithospheric thickness of 100 km, upper mantle viscosity 5×10^{20} Pa s, and lower mantle viscosity 5×10^{21} Pa s. The dotted and dashed black lines show the prediction using lateral variations in lithosphere alone and full 3D Earth structure (lithosphere plus mantle viscosity), respectively. C, D) Relative sea level using a 1D and 3D simulations along the same transect at different times during the deglaciation. E) Cross section of Earth structure along the transect from south to north. Viscosity perturbations are relative to the average upper mantle viscosity of 5×10^{20} Pa s.

343 for ocean island sites, which are generally situated on thinner oceanic lithosphere and can be underlain by lower
344 viscosity if their origin is plume related. Lithospheric thickness variations affect far-field sea-level indicators
345 more at the beginning of the LIG rather than the end (Fig. 5A,B) and in two specific ways: Firstly, thicker
346 lithosphere leads to continental levering over a broader area rather than being focused in a narrow corridor along
347 the coastlines. When the lithosphere is thicker on the landward side of the coastline, the continental levering
348 signal becomes asymmetric. One location that exemplifies this situation is Western Australia (7A, C). The
349 amount of continental levering when including lateral variations in lithospheric thickness in the calculation is
350 close to the 1D prediction on the oceanward side, where the lithosphere is only slightly thicker than 100 km.
351 However, predictions on the landward side are lower in amplitude and wider due to the thick (~200 km)
352 lithospheric root associated with the Yilgarn and Pilbara cratons (Fig. 7C). Secondly, large oceanic islands
353 generally experience more continental levering when lateral variations in lithospheric structure are considered
354 (Fig. 7D). This effect occurs because the lithosphere is typically thinner in oceanic settings than the 100 km
355 global average. For example, the Seychelles are part of a granitic plateau in the western Indian Ocean that was
356 exposed during the LGM and have a spatial extent of 50–100 km (Fig. 7B). The lithospheric thickness here
357 is around 80–90 km, and undergoes continental levering during exposure. Thinning the lithosphere further
358 causes the levering to become more pronounced, while increasing it to 100 km or higher results in the loss of
359 continental levering effects (Fig. 7D; Dendy *et al.*, 2017).

360 **Lateral variability in both lithospheric thickness and mantle viscosity.** Understanding the far-field
361 response to full 3D variability in Earth structure is challenging because far-field sea-level indicators are not
362 only sensitive to local Earth structure, but also to structure beneath the melting ice sheets and their periphery
363 and also to deeper mantle structure along the path between these ice sheets and the far-field site (Crawford
364 *et al.*, 2018). In Western Australia, we observe that including lateral viscosity variations leads to a smoother
365 continental levering signal (Fig. 7C). The 1D and 3D simulations exhibit long-wavelength, meter-amplitude
366 differences throughout the ocean basins, including a more positive sea level at the Seychelles (Fig. 7D). The
367 slightly less pronounced continental levering in the full 3D simulation is due to the higher than average viscosity
368 beneath the Seychelles plateau. Reducing the global average lithospheric thickness to 80 km instead of 100 km
369 (while keeping lateral variations in viscosity) allows for more deformation related to continental levering and
370 leads to an increased sea-level signal on the Seychelles plateau (Fig. 7D).

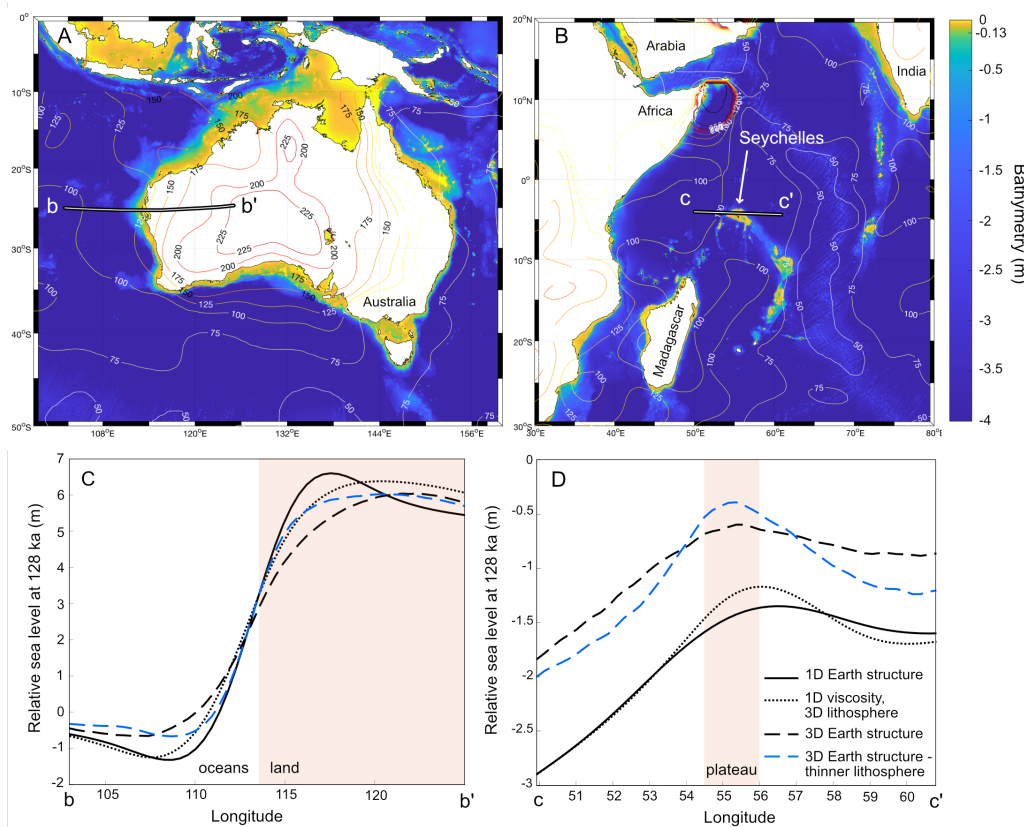


Figure 7: **Far-field GIA effects due to lateral variations in Earth structure.** A, B) Bathymetry around Australia and the Seychelles, respectively. Contour lines show lithospheric thickness in km. Relative sea level along the transects shown as black lines (b–b' and c–c') are displayed in panels C and D, respectively. C, D) Relative sea level is extracted at the beginning of the Last Interglacial (128 ka) and shown for simulations using a 1D Earth structure (black line) with a lithospheric thickness of 100 km, upper mantle viscosity 5×10^{20} Pa s, and lower mantle viscosity 5×10^{21} Pa s. The dotted and dashed black lines show predictions using lateral variations in lithosphere alone and full viscoelastic structure, respectively. The blue dashed line shows predictions using full 3D Earth structure (lithosphere plus mantle viscosity), but with a thinner lithosphere that has a global average of 80 km instead of 100 km.

371 **3.4 Predictions of 3D GIA at key LIG sites**

372 Next we consider predictions at specific sites that have notable records of LIG sea level (Fig. 8).

373 **Near-field locations.** Bermuda and Mallorca are located on the peripheral bulge of the former Laurentide
374 and Fennoscandian ice sheets, respectively. This forebulge subsides over the course of the LIG and therefore
375 leads to sea-level rise if GMSL is assumed to be constant (solid black lines, Fig. 8E, F). Accounting for lateral
376 variations in viscosity at Mallorca leads to a larger sea-level rise over the LIG (dashed black line, Fig. 8E).
377 Bermuda, on the other hand, is located in a region that is not strongly affected by lateral variations in viscosity
378 since the 1D and 3D predictions closely track one another (solid and dashed black line, Fig. 8E). We emphasise
379 that the ice history (and relative size) of the Fennoscandian and Laurentide ice sheets, which are not explored
380 here, will have a major affect on the GIA correction at these locations (Dendy *et al.*, 2017; Rohling *et al.*, 2017).

381 Ancient coral reefs in the Caribbean have long been used as paleo sea-level indicators. In particular,
382 records from Xcaret on the Yucatan Peninsula (Blanchon *et al.*, 2009) and various islands along the Bahamian
383 archipelago (e.g., Hearty *et al.*, 2007; Skrivanek *et al.*, 2018; Dyer *et al.*, in press.) have been influential due
384 to the existence of fossil corals with low age uncertainty and good preservation. Being located on the tail end
385 of the Laurentide peripheral bulge, these sites experience a small component of peripheral bulge subsidence (or
386 equivalent sea-level rise) in addition to continental levering. In both regions, the rate of sea-level rise is higher
387 in the 3D simulation, which might be related to a low viscosity in the asthenosphere (see section 3.2, Figs. 6, 5),
388 a trend that is particularly noticeable for the Yucatan Peninsula (Fig. 8C, D). Relative sea level predictions are
389 slightly reduced in the 3D GIA simulation that assumes a thinner lithosphere (blue dashed lines in Fig. 8C, D).
390 We also show predictions for Eleuthera in the northern Bahamas (yellow lines, Fig. 8D). For both 1D and 3D
391 simulations, GIA predictions at Eleuthera are significantly different from the prediction at Great Inagua, which
392 is expected given its location on the tail end of the peripheral bulge (Dyer *et al.*, in press.). These differences
393 demonstrate that applying a single GIA correction collectively to these sites is insufficient (Hearty *et al.*, 2007;
394 Clark *et al.*, 2020) and that they should each be individually corrected prior to comparison (Dyer *et al.*, in
395 press.).

396 **Far-field locations.** The Seychelles and Western Australia are located in the far field of the former major ice
397 sheets and have received substantial attention due to their high quality local sea-level reconstructions (Dutton
398 *et al.*, 2015b; O'Leary *et al.*, 2013). Our 1D LIG sea-level prediction in the Seychelles is relatively constant and
399 slightly below the global mean. Incorporating lateral variations in viscosity leads to a slight upwards shift by
400 0.5–1.0 m, which is the result of a combination of a slightly thinner lithosphere and lateral viscosity perturbations

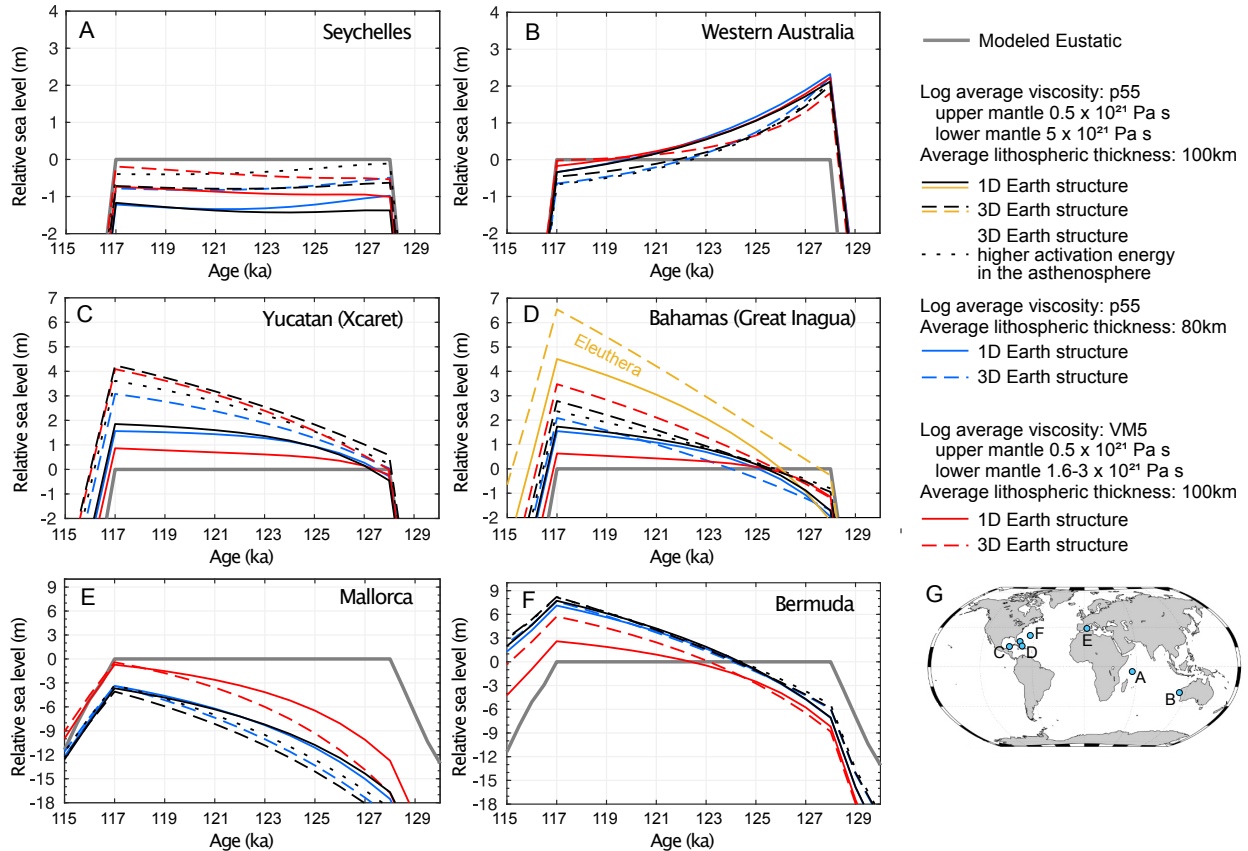


Figure 8: **GIA time series at key sites.** A-F) Local sea level at the Seychelles (La Digue), Western Australia (Cape Range), Yucatan Peninsula (Xcaret), Bahamas (Great Inagua and Eleuthera, Whale Point), Mallorca (Coves del Pirata), and Bermuda (Grape Bay), respectively. Thick gray line is the eustatic (global mean sea level) value assumed in the GIA model. Black lines show predictions of local sea level using a 1D (solid line) and 3D (dashed line, activation energy of 560 kJ mol^{-1} in the asthenosphere - dotted line) GIA model on top of the p55 average radial viscosity profile. The yellow line in panel D shows the 3D and 1D GIA predictions for Eleuthera (Bahamas) instead of Great Inagua (Bahamas). Blue lines are the same as black lines but use an average lithospheric thickness of 80 km. Red lines are the same as black lines but use the background 1D viscosity given by VM5 (Peltier *et al.*, 2015). G) Locations from A-F shown on a map.

401 (see section 3.3; Figs. 7; 8A). The Western Australian coast is located on a hinge point, with higher sea level
 402 predicted offshore and lower sea level predicted on land when comparing 3D and 1D simulations (section 3.3,
 403 Figs. 5, 7). As a result, predictions using lateral variations in Earth structure are quite close and only slightly
 404 lower than predictions using 1D Earth structure. At both far-field sites, relative sea level predictions are slightly
 405 increased at the beginning of the LIG and slightly decreased towards the end when assuming a 3D Earth model
 406 with a thinner lithosphere (blue dashed lines in Fig. 8A, B).

407 **4 Discussion**

408 The results presented above provide insight into the possible effects that lateral variations in lithospheric
 409 thickness and mantle viscosity can have on LIG sea level. Uncertainties remain in both the amplitude and
 410 pattern of viscosity perturbations, as we discuss in detail below. Ideally we would like to explore the full range
 411 of possible 3D Earth structures, however, this is currently not computationally feasible. On the other hand, 1D
 412 simulations are computationally inexpensive, and so we explore and discuss here two approximations: (1) we
 413 test whether the 3D effects (i.e. the difference between a 3D and 1D simulation, where the spherical average
 414 of the former is given by the latter) are consistent for different choices of 1D models; and (2) whether 3D GIA
 415 simulations can be approximated using 1D simulations where the 1D model differs from the spherical average
 416 of the 3D Earth model. We end our discussion by comparing our 3D GIA predictions to relative sea-level
 417 observations to understand how lateral variability in Earth structure may affect estimates of GMSL during the
 418 LIG.

419 **4.1 What are the uncertainties in Earth structure and how do they effect LIG GIA?**

420 There are three main factors that contribute to uncertainty in the mantle viscosity structure inferred from seismic
 421 tomography. The first involves the values of material properties that are used in the anelastic calibration (e.g.
 422 pressure- and temperature-dependence of the shear modulus and activation energy). The second is caused
 423 by inter-model differences in the seismic velocity structure imaged by different tomography studies. The third
 424 concerns the appropriate rheological deformation mechanism that is responsible for accommodating mantle flow
 425 during GIA. For the first two factors, our inverse anelastic calibration scheme provides a substantial advantage
 426 over traditional forward modelling approaches, which we illustrate in Fig. 9.

427 The traditional approach is to adopt material properties that have been measured in laboratory experiments
 428 and convert in a forward sense from seismic velocity to temperature and viscosity. Including the inherent
 429 uncertainties associated with these measurements introduces a spread in inferred Earth models. Our inverse
 430 calibration scheme, however, limits the number of acceptable combinations of material properties by retaining
 431 only those models that are consistent with the independent constraints on mantle structure (e.g. the thermal
 432 structure of oceanic lithosphere; Section 2.4.1). The approach reveals that there are trade-offs between the
 433 different material properties (Richards *et al.*, 2020). Whilst uncertainty in any individual parameter remains
 434 large, exploiting their co-variance results in a substantial reduction in the range of inferred Earth models.

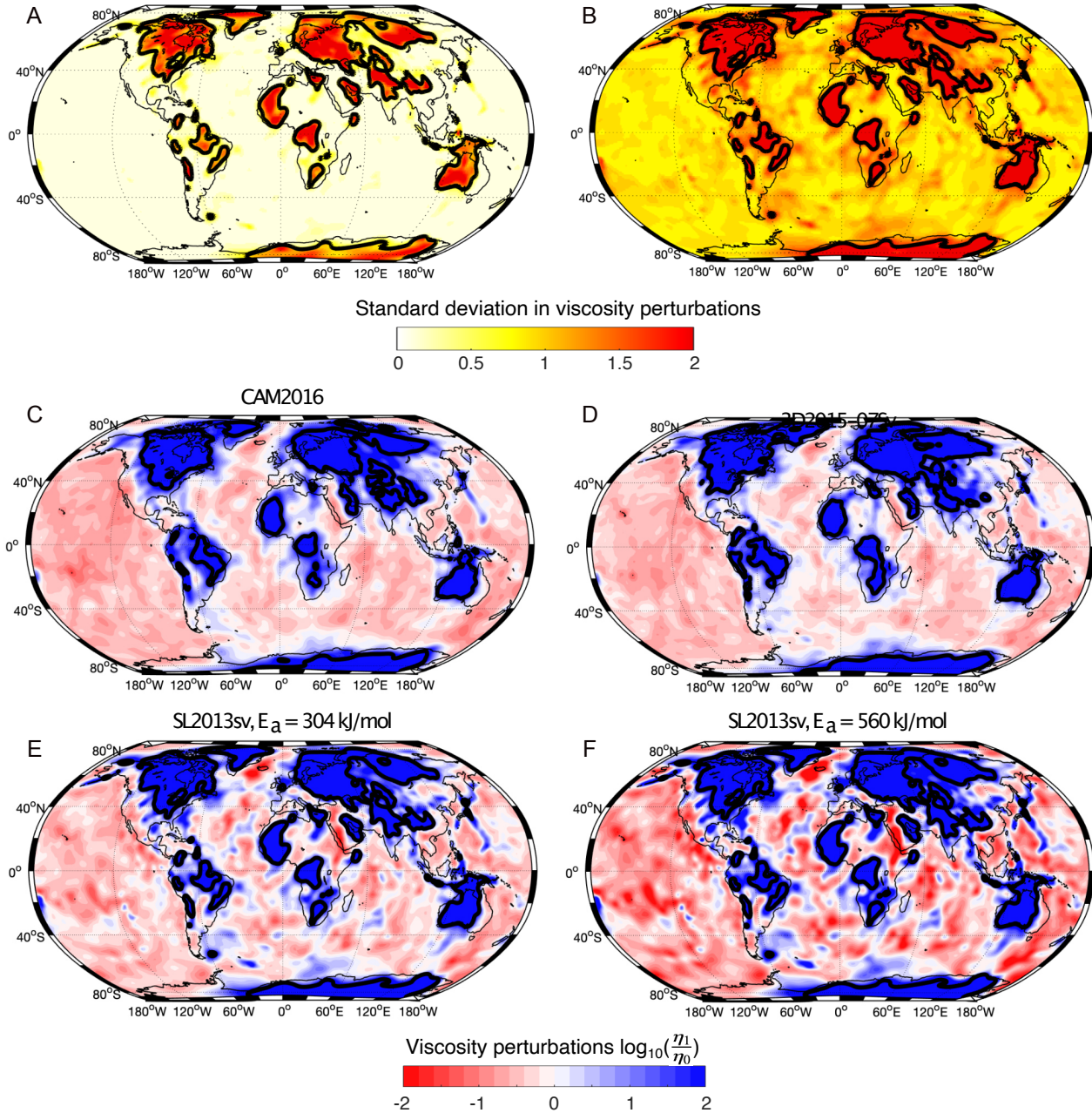


Figure 9: **Uncertainties in inferred Earth structure.** (A) Standard deviation in inferred diffusion creep viscosity at 175 km depth for one-thousand sets of anelastic parameters calibrated using the Richards *et al.* (2020) inversion scheme. Thick black line demarks lithosphere. (B) Same for a second suite of one thousand combinations of anelastic parameters, where each individual parameter is selected by randomly shuffling the values obtained in the construction of panel (A), forward mapped into viscosity. Uncertainties are larger in this traditional forward mapping scheme due to the absence of information on the covariance between anelastic parameters. (C) \log_{10} of the lateral viscosity perturbations at 175 km depth for an optimised calibration of CAM2016 seismic tomography model (Ho *et al.*, 2016; Priestley *et al.*, 2018). Thick black contour delineates the lithospheric portions. (D) As in (C), except for 3D2015-07Sv model (Debayle *et al.*, 2016). (E) As in (C), except for our preferred SL2013sv model (Schaeffer & Lebedev, 2013) and its optimal value of activation energy, $E_a = 304$ kJ mol⁻¹. (F) Same as (E), except that lateral temperature variations obtained from the calibrated anelastic parameterisation have been converted into viscosity using $E_a = 560$ kJ mol⁻¹, which is towards the upper end of the experimental range for dislocation creep in olivine.

435 We illustrate this key benefit using a simple test. The initial step of the anelasticity optimisation procedure
436 is a coarse parameter sweep that is designed to locate the approximate position of the global misfit minimum.
437 These parameters are then used as starting values in the second stage, which employs Powell's algorithm to
438 further minimise the misfit. For the test, we instead initiate this second stage from multiple different locations
439 within the parameter space, discarding the result if the final misfit value returned by the algorithm is not smaller
440 than the minimum value obtained in the coarse parameter sweep. In this manner, we obtain one thousand
441 different sets of optimised anelasticity parameters that all yield satisfactory fits to the independent constraints.
442 For each parameter, the range of optimal values across the one thousand sets is large and they remain individually
443 uncertain. Nevertheless, the resulting standard deviation across all one thousand inferred viscosity structures is
444 generally less than 0.2 orders of magnitude (Fig. 9A). Taking the set of one thousand values obtained for each
445 individual anelastic parameter in the calibration stage, we can randomly shuffle them and construct a second
446 suite of one thousand parameter combinations. This process yields the same total spread in individual material
447 properties but removes information concerning their covariance (i.e., the information concerning which value
448 of activation energy belongs with which value of reference viscosity, etc., is lost). Repeating the mapping
449 from shear-wave velocity to viscosity (this time in a forward sense), we find that there is an approximately five-
450 fold increase in the standard deviation of predicted viscosity models (Fig. 9B). Thus, our calibration scheme
451 substantially reduces the uncertainty in inferred mantle viscosity structure. Exploiting parameter covariance in
452 this manner is the strongest benefit of our inverse scheme over standard forward modelling practices.

453 The second source of uncertainty arises from differences in the starting seismic velocity structure between
454 different tomography models. Choices including tomographic inversion technique, data content, reference
455 velocity structure, and regularisation all introduce inter-model differences. Traditional forward mapping schemes
456 convert this variability into uncertainty in Earth structure. Our inverse calibration, however, reduces this
457 uncertainty because it requires each tomography model to individually yield a temperature structure that is
458 compatible with the independent constraints, thereby forcing some of the inter-model seismic velocity variation
459 into the resulting optimal anelastic parameters. In Fig.9C–E, we show results for three different surface wave
460 tomography models, where the third case is the one used in this study: CAM2016 (Ho *et al.*, 2016); 3D2015-07Sv
461 (Debayle *et al.*, 2016); and SL2013sv (Schaeffer & Lebedev, 2013). The resulting pattern of lateral viscosity
462 perturbations is relatively consistent between the three models, although the features in SL2013sv tend to be
463 slightly more localised and of higher amplitude in comparison to the other two. For each model, the root-
464 mean-squared value of lateral viscosity perturbations outside of the lithosphere is 0.84, 0.75, and 0.78 Pa s,

465 respectively. These values are more consistent with one another than the equivalent values obtained from
466 forward mapping each tomography model using the same set of material properties (0.68, 0.60, and 0.78 Pa s).

467 The third source of uncertainty, that concerning the rheological mechanism by which the mantle deforms
468 during GIA, is perhaps the most difficult to explore. The parameterisation for anelasticity at seismic frequencies
469 of Yamauchi & Takei (2016) yields a map of variations in the steady-state diffusion creep viscosity of the
470 mantle. This deformation mechanism is consistent with our assumption in the GIA simulations that the mantle
471 deforms like a Newtonian fluid. Nevertheless, it has also been suggested that deformation and flow during GIA
472 may occur via dislocation creep, particularly in locations where strain rates are highest in the comparatively
473 high-homologous-temperature asthenosphere (Huang *et al.*, 2019; van der Wal *et al.*, 2013). The dependence
474 of dislocation creep viscosity on temperature (i.e. activation energy) has generally been found to be higher in
475 laboratory experiments on olivine (430–570 kJ mol⁻¹ versus 240–425 kJ mol⁻¹; Karato & Wu, 1993; Hirth
476 & Kohlstedt, 2003; Fei *et al.*, 2012). Adopting mantle temperature variations obtained from the anelasticity
477 parameterisation, we see that applying this higher activation energy in the asthenosphere (between the lithosphere
478 and 300 km depth) would lead to larger lateral variations in viscosity (Fig.9F). We use this scenario to explore
479 the impacts of larger lateral viscosity variations on our sea-level reconstructions as might arise from dislocation
480 creep, while still assuming diffusion creep in our calculations.

481 Fully propagating uncertainties in viscosity into our GIA predictions is outside the scope of this work.
482 Nevertheless, in this and the following sections, we explore a few additional simulations. Using a viscosity
483 model with a larger activation energy in the asthenosphere leads to sub-meter changes in predicted sea level in
484 the far field (Fig. 10; dotted lines in Fig. 8). In the near field, where sensitivity extends deeper into the mantle
485 (where both models have the same viscosity variations), the difference in the two predictions is on the meter
486 scale, which is smaller than the sea-level change associated with introducing lateral variations in viscosity in
487 the first place (Fig. 5E, F).

488 **4.2 Are 3D GIA effects dependent on the average viscosity profile?**

489 Our default simulations (p55) use a lower mantle viscosity of 5×10^{21} Pa s, however Peltier *et al.* (2015) have
490 argued for a weaker viscosity at this depth. To explore the dependence of 3D GIA effects on the global average
491 viscosity, we repeat our simulations with the VM5 viscosity profile in which lower mantle viscosity varies from
492 $1.6\text{--}3.0 \times 10^{21}$ Pa s (Peltier *et al.*, 2015). GIA predictions using these two different 1D viscosity profiles can
493 differ significantly, especially in the near field (compare Fig. 11A,B to Fig. 4A,B). For example, the greater

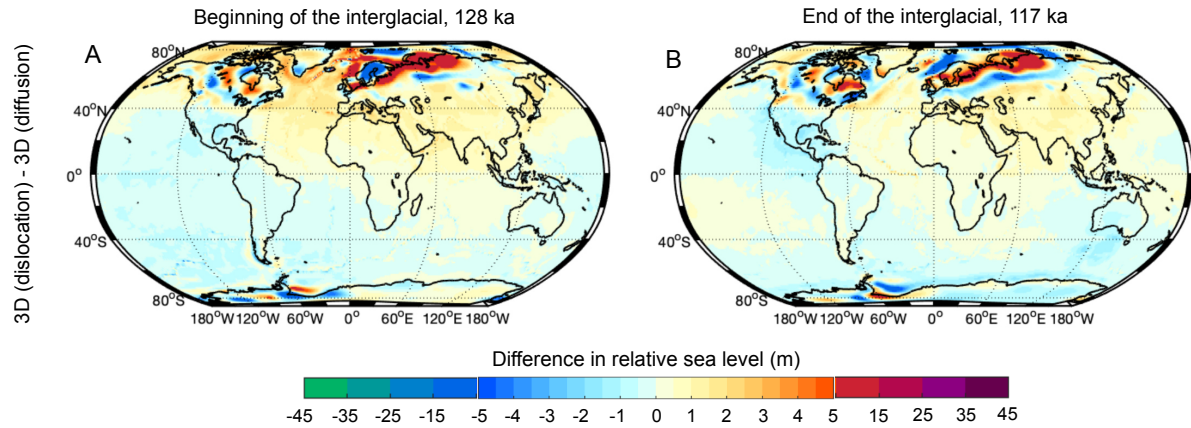


Figure 10: **Effect of larger activation energy in the asthenosphere.** A larger activation energy leads to higher amplitude viscosity variations, which is in line with expectations for dislocation creep, although we cannot explicitly model this rheology. A, B) Difference in relative sea level between a 3D viscosity model that uses a higher asthenospheric activation energy (above 300 km depth) and the reference case at the beginning (128 ka) and end (117 ka) of the Last Interglacial, respectively.

494 lower mantle viscosity in our default 1D predictions (p55) results in lower sea level at Mallorca and higher sea
 495 level at Bermuda, Bahamas and Yucatan, compared to simulations using the VM5 viscosity profile (red lines in
 496 Fig. 8). Differences are smaller in the far field at sites such as the Seychelles and Western Australia (~ tens of
 497 centimetres).

498 Using these results, we investigate whether the incorporation of lateral variations in viscosity has the same
 499 effect whether the p55 or VM5 depth average viscosity is adopted in the simulation. Note that the lateral
 500 variations in viscosity shown in Fig. 3 are superimposed on these two 1D profiles such that the spherical
 501 average of the logarithm of viscosity at each depth remains unaffected. Comparing the results in Fig. 5E, F to
 502 Fig. 11E, F indicates that the impact of lateral viscosity structure is qualitatively similar; however, differences
 503 in magnitude and geometry exist (Fig. 11G, H). This similarity is also evident when comparing results at
 504 specific locations: At Mallorca, for example, we find that while the choice of the 1D profile results in two
 505 different sea-level predictions (black versus red solid line in Fig. 8E), the signal due to the introduction of lateral
 506 variations is consistent (black and red dashed lines). On the peripheral bulge of the former Laurentide ice sheet,
 507 this signal has the same sign but differs in magnitude from site to site and is generally larger when adopting
 508 the VM5 viscosity profile. For example, at Bermuda, the sea-level predictions based on the p55 1D and 3D
 509 simulations are similar (within ~ 0.5 m; black solid versus dashed line in Fig. 8F), while the effect of adding
 510 lateral variations in viscosity is much larger when assuming the VM5 viscosity profile (+3 m towards the end of

511 the LIG; red solid versus dashed line in Fig. 8F). For the three sites in the vicinity of the Laurentide peripheral
512 bulge (Xcaret, Bahamas, and Bermuda), the two 3D predictions are more consistent with one another than their
513 associated 1D predictions, particularly for Xcaret where these differences remain less than 1 m throughout the
514 LIG (Fig. 8C, D, and F). In the far field, we find that the introduction of lateral variations in viscosity tends to
515 consistently increase local relative sea-level predictions at the Seychelles by up to ~ 1 m and decrease them by a
516 similar amount in Western Australia.

517 **4.3 Can 3D simulations be approximated with 1D simulations that are not the spherical average** 518 **of the 3D Earth model?**

519 Given the computational expense of 3D GIA simulations, it is worth investigating whether a simulation with a
520 suitable 1D viscosity profile, which is not necessarily the spherical average of the 3D Earth model, can be used to
521 approximate the 3D result with sufficient accuracy. Powell *et al.* (2019) considered synthetic GPS observations
522 in Antarctica and found that 1D simulations tuned to Earth structure local to the sites do not provide consistently
523 accurate approximations to the 3D synthetic predictions. Hartmann *et al.* (2020) have proposed an approach
524 which combines the result from different 1D simulations to approximate the 3D result. They focus on Antarctica
525 and argue that the approach has promise, but concede that it might be inaccurate in areas where the ice load and
526 sea-level observation are relatively distant from one another. The latter situation is the case for most sea-level
527 studies that consider observations distant from the former ice margins, such as the present study. Crawford
528 *et al.* (2018) used an adjoint approach to produce 3D sensitivity kernels that isolate regions of the mantle that
529 are sampled by a given sea-level record and whether increasing or decreasing viscosity in these regions will
530 lead to a better fit between the model prediction and the sea-level observation. They found that the sensitivity is
531 centred below the location of the sea-level record and extends towards the locations of ice melt. Moreover, their
532 time-dependent sensitivity kernels indicate that the region of greatest sensitivity will vary over time. These
533 results suggest that approximating 3D Earth structure using 1D simulations may be challenging. Nevertheless,
534 we explore two approaches here: First, we take a depth-average of the 3D Earth model in the vicinity of each
535 individual sea-level site (averaging is performed in logarithmic space and within a maximum distance of 3° of
536 the sea level site; Fig. 12A–F) and repeat our 1D simulations using this local structure. Second, we use a broad
537 suite of different viscosity profiles to assess whether any of them can provide a good approximation to the 3D
538 GIA result.

539 The locally averaged Earth structure obtained from the 3D model below the six key sea-level locations shows

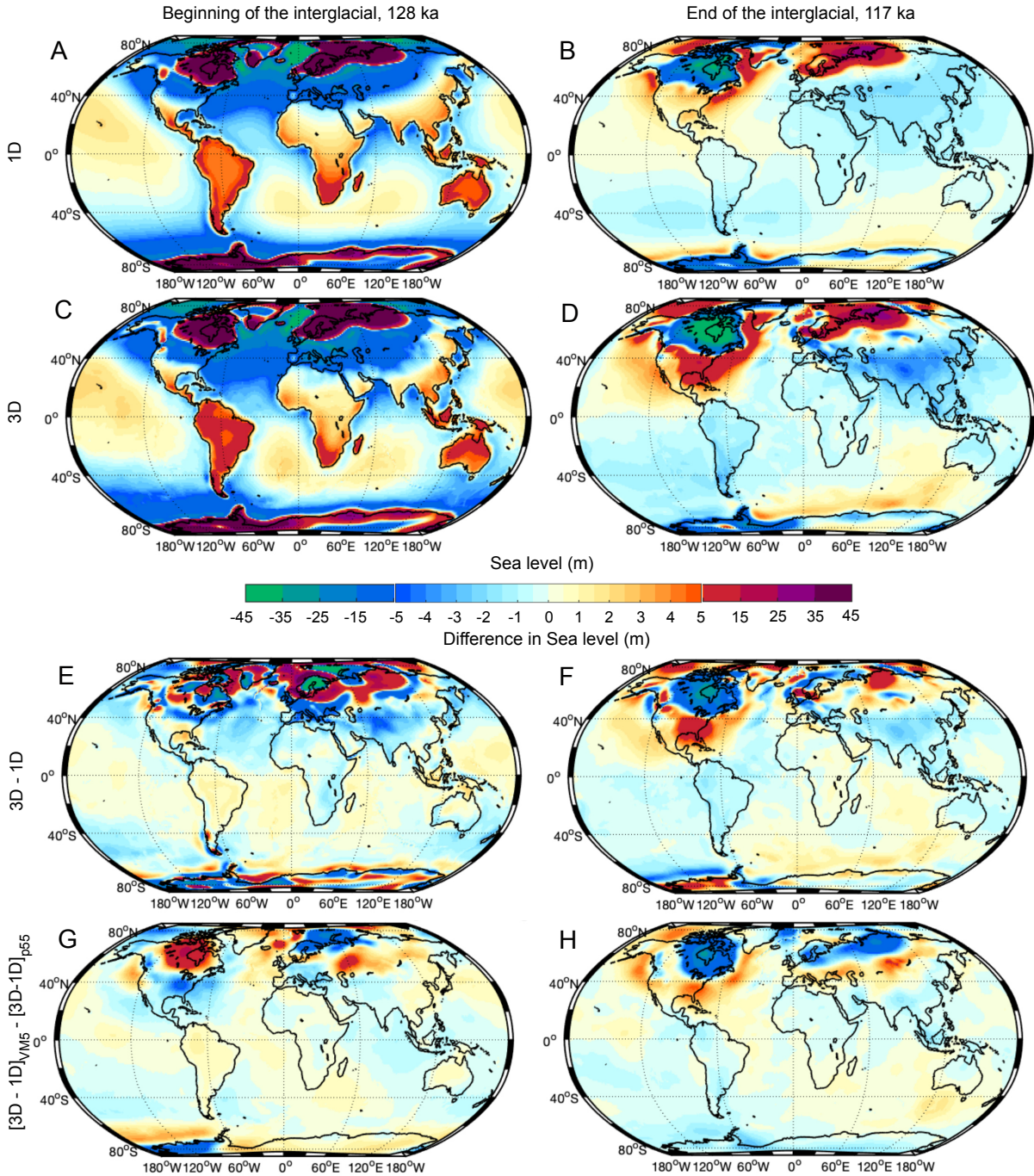


Figure 11: **Effect of the choice of the 1D background viscosity on LIG sea level.** A, B) Relative sea level at the beginning (128 ka) and end (117 ka) of the Last Interglacial, assuming the radially symmetric Earth structure VM5 (Peltier *et al.*, 2015). C, D) Same as A, B but including lateral variations in lithospheric thickness and mantle viscosity. E, F) Differences in relative sea level between model simulations that do and do not account for lateral variability in Earth structure. G, H) A comparison of the effect of lateral variations in viscosity when superimposed on the VM5 and p55 viscosity profiles. Plots show the difference in the 3D effect, i.e. the difference between panels E and F of this figure and panels E and F of Fig. 5

540 that most of them have a weaker than average upper mantle viscosity (Fig. 12A–F), which is not surprising
541 given that most of them are distant to subduction zones and cratonic regions. The only exception is Mallorca,
542 which has a higher than average viscosity in the deeper half of the upper mantle due the presence of a subducted
543 slab. Local viscosity variations in the lower mantle are more variable, with larger differences in particular in the
544 vicinity of the core-mantle boundary, which will have limited influence on the GIA response. Figures 12G–L
545 compare the result from the 1D simulations adopting local Earth structure (purple line) with the full 3D result
546 (black dashed line). The two results are consistent for the Yucatan peninsula (Fig. 12I), but do not agree well
547 elsewhere and exhibit particularly large deviations at the Seychelles.

548 We next test a range of 1D Earth models to investigate which (if any) structure approximates the local 3D
549 result for each site. We consider 48 different three-layer radial Earth models that each consist of an elastic
550 lithosphere overlying isoviscous upper and lower mantle regions. We systematically vary upper and lower
551 mantle viscosity across $3\text{--}5 \times 10^{20}$ Pa s and $3\text{--}40 \times 10^{21}$ Pa s, respectively, and test two different lithospheric
552 thicknesses (71 km and 96 km; see Fig. 12A). The range of all model simulations is shown in green in Fig.
553 12G–L. Sites in the far-field are most sensitive to lithospheric thickness variations and upper mantle viscosity
554 since continental levering is an important driver of sea level change for these sites. Sites on the peripheral bulge
555 of the former ice sheet are more sensitive to mantle viscosity: Great Inagua and Xcaret are most sensitive to
556 upper mantle viscosity, Mallorca is most sensitive to lower mantle viscosity, and Bermuda is equally sensitive
557 to upper and lower mantle viscosity. The detailed sensitivity is a function of distance between the sea level
558 location and the former ice sheet as well as the spatial extent of the former ice load.

559 We next compare our predictions for each 1D simulation to the 3D result at the six sites, calculating misfit
560 using the root-mean-square difference in relative sea level over the LIG (between 117 ka and 128 ka). The misfit,
561 which is shown as a function of upper and lower mantle viscosity in Fig. 12M–R, shows a strong dependence
562 on Earth structure for near-field sites (Fig. 12O–R) and a weaker dependency for far-field sites (Fig. 12M,N).
563 We find that the best fitting 1D Earth model at each site does produce a sea-level prediction that matches the
564 3D simulation reasonably well (green line compared to black dashed line in Fig. 12G–L). It is difficult to
565 compare the local Earth structure to the best-fitting 1D Earth structure given the coarse resolution of the latter,
566 however, the two show some consistency at far-field sites (green line compared to purple line in Fig. 12C–F).
567 Differences between the local and best fitting 1D Earth structure are expected given the broad sensitivity of
568 sea-level observations, which integrate Earth structure across wide regions of the mantle (Crawford *et al.*, 2018).
569 While the difference in the relative sea level prediction using a local structure versus the full 3D Earth structure

570 argues against using the former as an approximation for the 3D result, the suite of 1D results suggest that a
571 suitable 1D approximation may exist at each site. Inferring radial Earth structure from observations at these
572 sites would generally lead to overestimates of the average lower mantle viscosity. In other words, while the
573 global average viscosity in the lower mantle in these simulations is 5×10^{21} Pa s, the viscosity of the best fitting
574 1D model at all sites except for the Seychelles is higher than that value.

575 Finally, the above analysis raises the question: how useful is it to use a range of 1D viscosity models when
576 estimating uncertainties in the GIA correction (particularly uncertainties introduced by Earth structure)? The
577 green band in Fig. 12G–L shows the 1σ uncertainty range associated with the full ensemble of 1D Earth models
578 used here (the mean is not shown, but it sits in the middle of the light green band). In the near field, the 3D
579 result falls within the range of 1D predictions (Fig. 12I–L). In the far field, the uncertainty range is relatively
580 narrow and the 3D prediction falls just outside of this 1σ range, but within the 2σ range (Fig. 12G, H, note that
581 the 2σ is not shown). We thus consider that results based on a range of 1D model runs may provide a suitable
582 estimate of the uncertainty associated with the potential signal from lateral variations in viscosity structure.

583 **4.4 How do lateral variations in Earth structure affect estimates of Last Interglacial global** 584 **mean sea level?**

585 Estimates of GMSL during the LIG are based on sea-level observations (such as corals or speleothems) from
586 this time period. The locations we have chosen for our investigation (Fig. 8, 13) are among the sites with the
587 most reliable local sea-level records. The inferred GMSL estimate at each site is given by the difference between
588 observed sea level and that predicted by the GIA simulation. Sea level during the LIG will also vary spatially
589 depending on which ice sheet is driving the excess melting (Hay *et al.*, 2014), an issue which is not explored
590 here.

591 In Mallorca, phreatic overgrowths on speleothems (POS) have been used to reconstruct local sea level,
592 which the authors infer to be relatively stable throughout the LIG (Polyak *et al.*, 2018; Fig. 13E). Given that
593 relative sea level is predicted to steadily rise due to GIA, Polyak *et al.* (2018) concluded that GMSL must be
594 falling over the LIG in order to result in constant relative sea level. Our result indicates that an even greater
595 fall of sea level would be required if lateral variations in viscosity are accounted for (Fig. 13E). Bermuda is
596 the other near-field site in our analysis, and stratigraphic and coral evidence suggests that local sea level peaked
597 around 6–8 m above present; however the exact timing and evolution is controversial due to insufficient age
598 control (Hearty, 2002; Muhs *et al.*, 2020). Accounting for lateral variations in viscosity will tend to reduce the

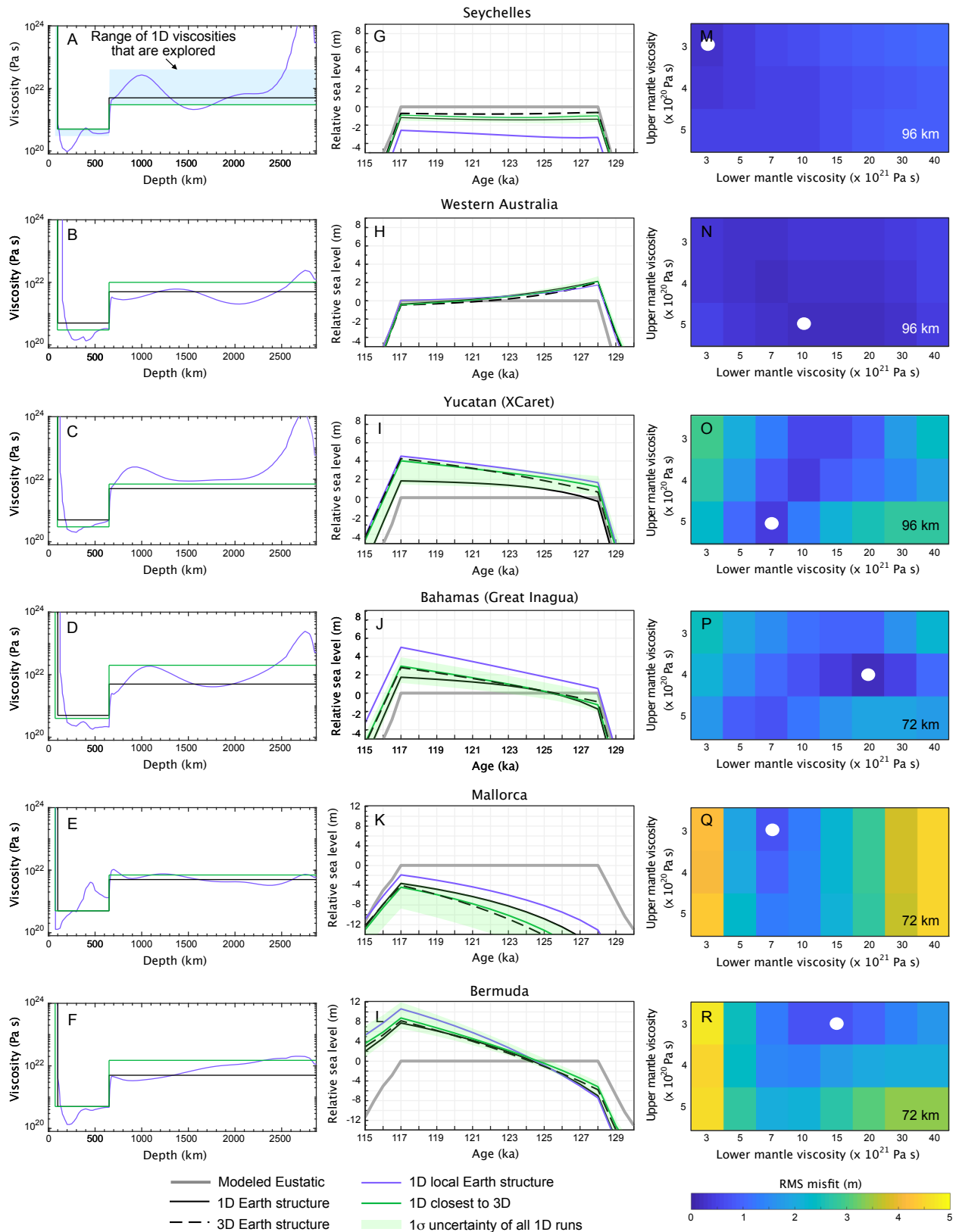


Figure 12: (Caption next page.)

Figure 12: (Figure previous page.) **Approximating 3D Earth structure with radially symmetric structure.** A–F) Locally averaged viscosity structure as a function of depth from the 3D Earth model (purple), global average viscosity (black), and 3-layer 1D viscosity profile that best fits the 3D GIA prediction at each location (green). Light green band in panel A shows the full range of 1D models explored here. To compute the locally averaged viscosity structure, the viscosity below the site was averaged across a maximum distance of 3° from the sea level site at each depth. G–L) Local relative sea-level predictions at selected sites (see caption of Fig. 8 for exact locations) using the 1D viscosity profiles shown in panels A–F with the same colours and also including predictions for the full 3D Earth structure (black dashed line). Thick gray line is the global mean sea-level value assumed in the GIA model. Light green range marks the 1σ uncertainty range for the ensemble of 1D runs explored here. M–R) Parameter sweeps through upper and lower mantle viscosity (see text) at optimal lithospheric thickness for each site, showing misfit between each individual 1D prediction and the 3D prediction. The optimal lithospheric thickness is noted in the bottom right corner of each panel. The Earth model with the minimum misfit is shown by the white circle (this model is given by the green line in panels A–F).

599 magnitude of the inferred GMSL and, assuming that the highstand was recorded late in the LIG, implies only a
600 few meters of excess GMSL during that time.

601 More distal near-field records from the Yucatan Peninsula and the Bahamas show locally rising sea level,
602 which are recorded by extensive coral reefs. At the ecological park of Xcaret, Blanchon *et al.* (2009) identified
603 a lower and upper reef crest (Fig. 13C). In the Bahamas, Dyer *et al.* (in press.) used coral and sedimentary
604 evidence combined with a large suite of radially symmetric Earth models to calculate a posterior relative sea-
605 level history that exhibits an early sea-level rise, followed by slightly falling sea level before culminating in a
606 final rise (Fig. 13D). This history is in agreement with earlier analyses from this location (Skrivanek *et al.*,
607 2018; Dutton & Lambeck, 2012). If one were to assume 1D Earth structure at these locations, one would infer
608 $\sim 3\text{--}4$ m of excess GMSL early and late in the interglacial, with a GMSL lowstand in the interim. The 3D GIA
609 predictions are higher than the 1D predictions towards the end of the LIG, which may lower the inferred GMSL
610 at the end of the LIG.

611 Far-field records along the western coast of Australia and in the Seychelles are also based on coral outcrops.
612 O’Leary *et al.* (2013) dated corals at several locations in Western Australia and inferred an early rise in local sea
613 level that was followed by a GIA-driven sea-level fall, which resulted in erosion of a coral platform (Fig. 13B).
614 Additional higher corals were interpreted to reflect a late rise in sea level. Dutton & Lambeck (2012) inferred
615 a similar planated surface during the first half of the LIG and interpreted the higher corals to be tectonically
616 deformed (see also Sandstrom *et al.*, 2020). GIA and therefore inferred GMSL would be marginally impacted
617 by 3D Earth structure at this location, which tends to increase inferred GMSL (by ~ 0.5 m). Inferred GMSL is
618 $3\text{--}4$ m at the beginning of the LIG (in line with earlier estimates) and remains at that level to the end of the LIG
619 if the high corals are discounted or increases to ~ 9 m if they are not. Lastly, extensive coral reefs are absent on

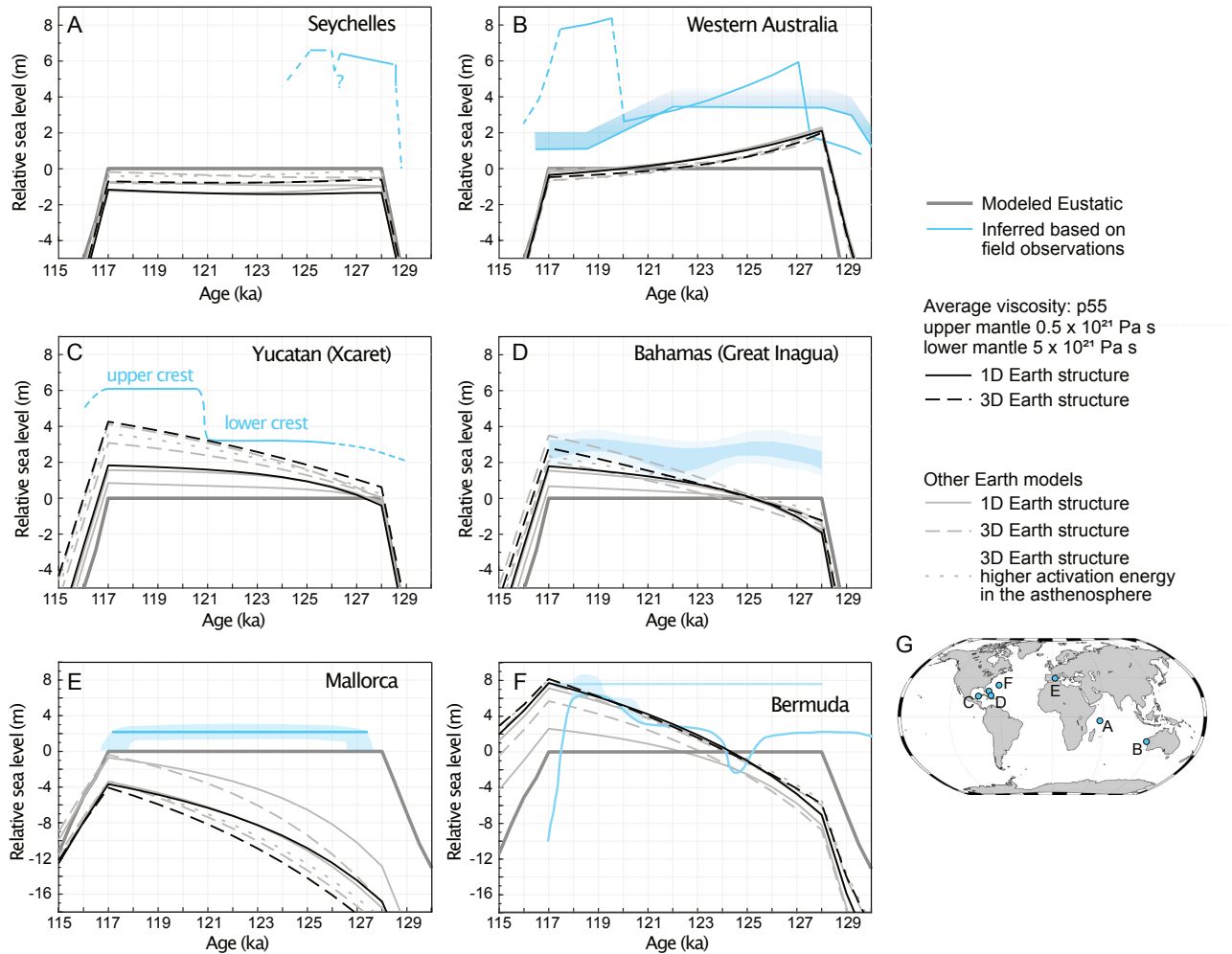


Figure 13: **GIA time series at key sites with LIG sea-level records.** A-F) Relative sea level at the Seychelles (La Digue), Western Australia (Cape Range), Yucatan Peninsula (Xcaret), Bahamas (Great Inagua and Eleuthera, Whale Point), Mallorca (Coves del Pirata), and Bermuda (Grape Bay), respectively. Thick grey line is the eustatic (global mean sea level) value assumed in the GIA model. Thus, any predicted relative sea-level change during the LIG can only be due to GIA and not global mean sea-level changes. Black lines show predictions of relative sea level using a 1D (solid line) and the 3D (dashed line) GIA model with spherical average given by the p55 viscosity profile. Grey lines are results for different 1D and 3D Earth models from Fig. 8. Light blue lines show the inferred relative sea level at each site based on a variety of observations, with shaded regions marking uncertainties cited in the original publications: Seychelles (Dutton *et al.*, 2015b); Western Australia, line without uncertainty (O’Leary *et al.*, 2013) and line with uncertainty (Dutton & Lambeck, 2012); Yucatan (Blanchon *et al.*, 2009); Bahamas, with 1σ and 2σ uncertainty (Dyer *et al.*, in press.); Mallorca (Polyak *et al.*, 2018); and Bermuda, time-varying prediction (Hearty, 2002) and constant prediction based on the highest reported Devonshire marine member which has large age uncertainties (Muhs *et al.*, 2020). G) Locations from A-F shown on a map.

620 the Seychelles, but individual corals and coralline algae are attached to granitic bedrock (Dutton *et al.*, 2015b;
621 Vyverberg *et al.*, 2018) and found at high elevations, leading to an interpreted local sea level of around 6–7 m
622 above present early in the LIG (Dutton *et al.*, 2015b). 3D GIA results tend to increase the predicted relative
623 sea level, which decreases the inferred GMSL (Fig. 13A). The magnitude of this effect ranges from 0.5–1.5 m
624 (where this range includes the simulation with a larger activation energy in the asthenosphere) leading to an
625 inferred GMSL early in the LIG that remains larger than that at most other sites (6–7.5 m). Increasing the GIA
626 prediction for local relative sea level (and hence reducing the inferred GMSL) is possible by decreasing the
627 lithospheric thickness in this region (Fig. 7), which enhances continental levering. However, this effect would
628 also be expected to occur during the Holocene and would result in an early Holocene sea-level highstand, which
629 has not been observed (Woodroffe *et al.*, 2015).

630 Inferences of GMSL during the LIG described above are based on a limited number of 3D simulations,
631 and a rigorous analysis would require testing a significantly larger suite of Earth structures. In addition to
632 Earth structure, there are several major uncertainties associated with the ice history that are not explored in this
633 analysis, but will be briefly summarised: (1) The calculations performed here begin at 150 ka (Fig. 1), which
634 assumes that the ice-Earth system was in isostatic equilibrium at this time. We have performed 1D simulations
635 that include earlier glacial cycles and found that this effect is on the order of 1 m in areas of the peripheral bulge
636 and smaller (decimetre scale) in the far field; (2) GIA across the LIG will be sensitive to the specific ice sheet
637 configuration adopted during the penultimate deglaciation, an uncertainty explored in detail elsewhere (Dendy
638 *et al.*, 2017; Rohling *et al.*, 2017), and this factor will be particularly crucial to consider when attempting to
639 reconcile relatively near-field sites such as Mallorca and Bermuda; (3) GIA predictions of relative sea level
640 during the LIG are also sensitive to the ice history during the last glacial cycle (Lambeck *et al.*, 2012). Here,
641 we have assumed that sea level was relatively high during MIS 3 due to a small Laurentide ice sheet, following
642 the results of Pico *et al.* (2017). If we were to assume that the Laurentide ice sheet was larger during MIS 3,
643 it would lead to a further increase in predicted relative sea level during the LIG at sites close to the former
644 Laurentide ice sheet; (4) Ice melt during the LIG will drive spatially variable sea level changes, and this should
645 be accounted for when comparing GMSL inferences from different locations (Hay *et al.*, 2014).

646 **5 Conclusion**

647 In this study we describe GIA predictions based on a new model of Earth's 3D viscoelastic structure inferred from
648 recent global tomographic models (Schaeffer & Lebedev, 2013, 2014; French & Romanowicz, 2014). We use
649 an upper mantle anelastic parameterisation that relates shear wave speed to diffusion creep viscosity and is based
650 on laboratory deformation experiments (Yamauchi & Takei, 2016). The parameters within these relationships
651 are calibrated such that the resulting temperature variations match a series of independent observables (Richards
652 *et al.*, 2020) and this reduces the uncertainty in the inferred viscosity. We note that the apparent viscosity over
653 ice age timescales might deviate from the steady-state viscosity due to transient behaviour (Lau & Holtzman,
654 2019), which is not explored here.

655 We use this new model of Earth's internal structure to produce the first estimates of GIA-driven sea-level
656 change across the LIG that incorporate lateral variations in viscoelastic structure. We find that GIA predictions
657 of relative sea level based on 3D versus 1D Earth structure have meter-scale differences in both the near and
658 far field. We explore the mechanisms responsible for these differences and demonstrate how effects such as
659 forebulge dynamics and continental levering are influenced by the presence of lateral variations in lithospheric
660 thickness and underlying mantle viscosity. A more detailed examination of these differences is possible using
661 3D sensitivity kernels (Al-Attar & Tromp, 2014; Crawford *et al.*, 2018).

662 The effect that lateral viscosity variations have on sea level is weakly dependent on the globally averaged
663 1D viscosity structure that these variations are superimposed on: Using two different 1D profiles, we find that
664 the difference between 3D and 1D predictions of LIG sea level differ more in magnitude than in geographic
665 pattern. Thus, our results can be used as a first-order guide to whether lateral mantle viscosity variations might
666 increase or decrease relative sea level in comparison to 1D GIA predictions.

667 Given the computational expense of 3D GIA simulations, it is important to consider if and how well such
668 simulations can be approximated by 1D GIA modelling. We find that 1D simulations that assume local Earth
669 structure within a 3° radius of the site do not produce results that are representative of the 3D result, which is
670 consistent with earlier findings (Powell *et al.*, 2019; Hartmann *et al.*, 2020). However, a suite of 1D simulations
671 suggests that a suitable and unique 1D approximation may exist for each site and we speculate that appropriate
672 values for such a model might be found by averaging 3D structure over mantle regions characterised by high
673 sensitivity (Crawford *et al.*, 2018).

674 Lastly, we compare our predictions of GIA for 3D Earth models to local LIG sea-level reconstructions to

675 investigate the implications of such models for estimates of GMSL during the LIG. It is noteworthy that lateral
676 variations in mantle viscosity perturb predictions in a manner that may help to reconcile the mismatch in inferred
677 GMSL early in the LIG from the Seychelles, where they lower this value, and western Australia, where they
678 increase it. However, this effect is relatively small in the models described here (0.5–1.5 m) and insufficient to
679 bring published estimates from these two sites into accord. In any event, our results show that lateral variations
680 in Earth structure are important to consider when reconstructing past sea level and estimating peak GMSL (or
681 minimum ice volumes) during periods of relative ice age warmth.

682 **Acknowledgments**

683 This work has been supported by the National Science Foundation under grant OCE 18-41888 and ICER
684 19-28146 (JA) and OCE 17-02684 (JXM). MH and JXM acknowledge support from the National Aeronautics
685 and Space Administration (grant NNX17AE17G). MH acknowledges support from the Australian government's
686 Exploring for the Future program. FDR acknowledges support from the Schmidt Science Fellows program, in
687 partnership with the Rhodes Trust, and the Imperial College Research Fellowship scheme. We are grateful to
688 Tamara Pico for providing her ice reconstruction for MIS 3 to MIS 5d, Sia Ghelichkhan for discussions concern-
689 ing conversion of seismic velocities into Earth structure, and Andrew Lloyd for discussions about sensitivity
690 kernels and general feedback. The authors acknowledge PALSEA, a working group of the International Union
691 for Quaternary Sciences (INQUA) and Past Global Changes (PAGES), which in turn received support from the
692 Swiss Academy of Sciences and the Chinese Academy of Sciences. Supplementary datasets are available with
693 the online version of this manuscript and in the accompanying OSF database (<https://osf.io/XXXXXX>).

694 **Author contributions**

695 JA designed the research and performed the sea-level analysis with input from all authors. MH and FDR
696 performed conversions from shear wave speed to temperature and explored related uncertainties. KL performed
697 the 3D GIA calculations and JA performed the 1D GIA calculations. JA and MH wrote the majority of the
698 manuscript with input from all authors.

699 **Appendix A: Anelastic parameterisation**

700 The anelastic parameterisation of Yamauchi & Takei (2016) represents linear viscoelasticity in the frequency
701 domain using a complex compliance, the real component of which refers to the amplitude of strain that occurs in

702 phase with the driving stress and the imaginary component refers to strain that is $\pi/2$ radians out of phase (and
703 gives rise to dissipation). Processes responsible for accommodating anelastic deformation are represented using
704 a relaxation spectrum that consists of a high-frequency peak superimposed on top of a monotonic background.
705 The height and width of the high-frequency peak is a function of the material's homologous temperature, $\frac{T}{T_m}$.
706 The background takes advantage of the Maxwell frequency "master variable" scaling results of McCarthy *et al.*
707 (2011), which crucially showed that the effects of variations in composition, grain size, and temperature on
708 attenuation can be accurately predicted using the corresponding effect of these parameters on the steady-state
709 diffusion creep viscosity of the material.

710 In their laboratory experiments on organic rock-analogues, Yamauchi & Takei (2016) were able to ascertain
711 the values of several anelastic parameters that are thought to be consistent between different polycrystalline
712 materials (e.g. the centre frequency of the relaxation peak). Seven other parameters are specific to each
713 individual material and need to be independently determined. These include the unrelaxed shear modulus
714 at reference conditions, its dependence on temperature and pressure, the viscosity at reference conditions
715 (1200°C and 1.5 GPa), its dependence on temperature and pressure (activation energy and activation volume,
716 respectively), and the solidus gradient. Assuming that suitable values for these parameters can be ascertained,
717 the parameterisation allows shear wave velocities to be converted into temperature and steady-state diffusion
718 creep viscosity in a self-consistent manner. The exact form used in this study is given by Equations (3)–(17) of
719 Richards *et al.* (2020).

720 **References**

- 721 Al-Attar, D. & Tromp, J., 2014. Sensitivity kernels for viscoelastic loading based on adjoint methods, *Geophys-*
722 *ical Journal International*, **196**(1), 34–77.
- 723 Andrault, D., Bolfan-Casanova, N., Nigro, G. L., Bouhifd, M. A., Garbarino, G., & Mezouar, M., 2011. Solidus
724 and liquidus profiles of chondritic mantle: Implication for melting of the Earth across its history, *Earth and*
725 *Planetary Science Letters*, **304**, 251–259.
- 726 Austermann, J., Mitrovica, J. X., Latychev, K., & Milne, G. A., 2013. Barbados-based estimate of ice volume
727 at Last Glacial Maximum affected by subducted plate, *Nature Geoscience*, **6**(7), 553–557.
- 728 Austermann, J., Mitrovica, J. X., Huybers, P., & Rovere, A., 2017. Detection of a dynamic topography signal in
729 last interglacial sea-level records, *Science Advances*, **3**(7), e1700457.
- 730 Barlow, N. L. M., McClymont, E. L., Whitehouse, P. L., Stokes, C. R., Jamieson, S. S. R., Woodroffe, S. A.,
731 Bentley, M. J., Callard, S. L., Cofaigh, C. Ó., Evans, D. J. A., Horrocks, J. R., Lloyd, J. M., Long, A. J.,
732 Margold, M., Roberts, D. H., & Sanchez-Montes, M. L., 2018. Lack of evidence for a substantial sea-level
733 fluctuation within the last interglacial, *Nature Geoscience*, **11**(9), 627–634.
- 734 Blanchon, P., Eisenhauer, A., Fietzke, J., & Liebtrau, V., 2009. Rapid sea-level rise and reef back-stepping at
735 the close of the last interglacial highstand, *Nature*, **458**(7240), 881–884.
- 736 Briggs, R. W., Engelhart, S. E., Nelson, A. R., Dura, T., Kemp, A. C., Haeussler, P. J., Corbett, D. R., Angster,
737 S. J., & Bradley, L.-A., 2014. Uplift and subsidence reveal a nonpersistent megathrust rupture boundary
738 (sitkinak island, alaska), *Geophysical Research Letters*, **41**(7), 2289–2296.
- 739 Bullen, K. E., 1975. *The Earth's density*, Springer, London.
- 740 Cammarano, F., Goes, S., Vacher, P., & Giardini, D., 2003. Inferring upper-mantle temperatures from seismic
741 velocities, *Physics of the Earth and Planetary Interiors*, **138**, 197–222.
- 742 Cathles, L. M., 1975. *Viscosity of the Earth's mantle*, Princeton University Press, Princeton.
- 743 Clark, P. U., He, F., Gollledge, N. R., Mitrovica, J. X., Dutton, A., Hoffman, J. S., & Dendy, S., 2020. Oceanic
744 forcing of penultimate deglacial and last interglacial sea-level rise, *Nature*, **577**(7792), 660–664.

- 745 Colleoni, F., Wekerle, C., Näslund, J.-O., Brandefelt, J., & Masina, S., 2016. Constraint on the penultimate
746 glacial maximum northern hemisphere ice topography (≈ 140 kyrs BP), *Quaternary Science Reviews*, **137**,
747 97–112.
- 748 Connolly, J. A., 2005. Computation of phase equilibria by linear programming: A tool for geodynamic modeling
749 and its application to subduction zone decarbonation, *Earth and Planetary Science Letters*, **236**, 524–541.
- 750 Crawford, O., Al-Attar, D., Tromp, J., Mitrovica, J. X., Austermann, J., & Lau, H. C. P., 2018. Quantifying the
751 sensitivity of post-glacial sea level change to laterally varying viscosity, *Geophysical Journal International*,
752 **214**(2), 1324–1363.
- 753 Creveling, J. R., Mitrovica, J. X., Clark, P. U., Waelbroeck, C., & Pico, T., 2017. Predicted bounds on peak
754 global mean sea level during marine isotope stages 5a and 5c, *Quaternary Science Reviews*, **163**, 193–208.
- 755 Dalton, C. A., Ekström, G., & Dziewonski, A. M., 2009. Global seismological shear velocity and attenuation:
756 A comparison with experimental observations, *Earth and Planetary Science Letters*, **284**(1-2), 65–75.
- 757 Dannberg, J., Eilon, Z., Faul, U., Gassmöller, R., Moulik, P., & Myhill, R., 2017. The importance of grain
758 size to mantle dynamics and seismological observations, *Geochemistry, Geophysics, Geosystems*, **18**(8),
759 3034–3061.
- 760 Debayle, E., Dubuffet, F., & Durand, S., 2016. An automatically updated s-wave model of the upper mantle and
761 the depth extent of azimuthal anisotropy, *Geophysical Research Letters*, **43**(2), 674–682.
- 762 DeConto, R. M. & Pollard, D., 2016. Contribution of antarctica to past and future sea-level rise, *Nature*,
763 **531**(7596), 591–597.
- 764 Dendy, S., Austermann, J., Creveling, J., & Mitrovica, J., 2017. Sensitivity of last interglacial sea-level high
765 stands to ice sheet configuration during marine isotope stage 6, *Quaternary Science Reviews*, **171**, 234–244.
- 766 Dutton, A. & Lambeck, K., 2012. Ice volume and sea level during the last interglacial, *Science*, **337**(6091),
767 216–219.
- 768 Dutton, A., Carlson, A. E., Long, A. J., Milne, G. A., Clark, P. U., DeConto, R., Horton, B. P., Rahmstorf, S.,
769 & Raymo, M. E., 2015. Sea-level rise due to polar ice-sheet mass loss during past warm periods, *Science*,
770 **349**(6244), aaa4019–aaa4019.

- 771 Dutton, A., Webster, J. M., Zwartz, D., Lambeck, K., & Wohlfarth, B., 2015. Tropical tales of polar ice:
772 evidence of last interglacial polar ice sheet retreat recorded by fossil reefs of the granitic seychelles islands,
773 *Quaternary Science Reviews*, **107**, 182–196.
- 774 Dyer, B., Austermann, J., D’Andrea, W. J., Creel, R. C., Sandstrom, M. R., Cashman, M., Rovere, A., & Raymo,
775 M. E., in press. Sea level trends across the bahamas constrain peak last interglacial ice melt, *PNAS*.
- 776 Dziewonski, A. M. & Anderson, D. L., 1981. Preliminary reference Earth model, *Physics of the Earth and*
777 *Planetary Interiors*, **25**(4), 297–356.
- 778 Faul, U. & Jackson, I., 2015. Transient Creep and Strain Energy Dissipation: An Experimental Perspective,
779 *Annual Review of Earth and Planetary Sciences*, **43**, 541–569.
- 780 Fei, H., Hegoda, C., Yamazaki, D., Wiedenbeck, M., Yurimoto, H., Shcheka, S., & Katsura, T., 2012. High
781 silicon self-diffusion coefficient in dry forsterite, *Earth and Planetary Science Letters*, **345-348**, 95–103.
- 782 Fei, H., Wiedenbeck, M., Sakamoto, N., Yurimoto, H., Yoshino, T., Yamazaki, D., & Katsura, T., 2018. Negative
783 activation volume of oxygen self-diffusion in forsterite, *Physics of the Earth and Planetary Interiors*, **275**,
784 1–8.
- 785 Fichtner, A., Trampert, J., Cupillard, P., Saygin, E., Taymaz, T., Capdeville, Y., & Villaseñor, A., 2013.
786 Multiscale full waveform inversion, *Geophysical Journal International*, **194**(1), 534–556.
- 787 Fischer, H., Meissner, K. J., Mix, A. C., Abram, N. J., Austermann, J., Brovkin, V., Capron, E., Colombaroli,
788 D., Daniau, A.-L., Dyez, K. A., Felis, T., Finkelstein, S. A., Jaccard, S. L., McClymont, E. L., Rovere, A.,
789 Sutter, J., Wolff, E. W., Affolter, S., Bakker, P., Ballesteros-Cánovas, J. A., Barbante, C., Caley, T., Carlson,
790 A. E., Churakova, O., Cortese, G., Cumming, B. F., Davis, B. A. S., de Vernal, A., Emile-Geay, J., Fritz,
791 S. C., Gierz, P., Gottschalk, J., Holloway, M. D., Joos, F., Kucera, M., Loutre, M.-F., Lunt, D. J., Marcisz, K.,
792 Marlon, J. R., Martinez, P., Masson-Delmotte, V., Nehrbass-Ahles, C., Otto-Bliesner, B. L., Raible, C. C.,
793 Risebrobakken, B., Goñi, M. F. S., Arrigo, J. S., Sarnthein, M., Sjolte, J., Stocker, T. F., Álvarez, P. A. V.,
794 Tinner, W., Valdes, P. J., Vogel, H., Wanner, H., Yan, Q., Yu, Z., Ziegler, M., & Zhou, L., 2018. Palaeoclimate
795 constraints on the impact of 2 °c anthropogenic warming and beyond, *Nature Geoscience*, **11**(7), 474–485.
- 796 French, S. W. & Romanowicz, B. A., 2014. Whole-mantle radially anisotropic shear velocity structure from
797 spectral-element waveform tomography, *Geophysical Journal International*, **199**(3), 1303–1327.

- 798 Goldberg, S. L., Lau, H. C., Mitrovica, J. X., & Latychev, K., 2016. The timing of the black sea flood event:
799 Insights from modeling of glacial isostatic adjustment, *Earth and Planetary Science Letters*, **452**, 178–184.
- 800 Gomez, N., Latychev, K., & Pollard, D., 2018. A coupled ice sheet–sea level model incorporating 3d earth
801 structure: Variations in antarctica during the last deglacial retreat, *Journal of Climate*, **31**(10), 4041–4054.
- 802 Hartmann, R., Ebbing, J., & Conrad, C., 2020. A multiple 1d earth approach (m1dea) to account for lateral
803 viscosity variations in solutions of the sea level equation: An application for glacial isostatic adjustment by
804 antarctic deglaciation, *Journal of Geodynamics*, **135**, 101695.
- 805 Hay, C., Mitrovica, J., Gomez, N., Creveling, J., Austermann, J., & Kopp, R., 2014. The sea-level fingerprints
806 of ice-sheet collapse during interglacial periods, *Quaternary Science Reviews*, **87**, 60–69.
- 807 Hearty, P. J., 2002. Revision of the late pleistocene stratigraphy of bermuda, *Sedimentary Geology*, **153**(1-2),
808 1–21.
- 809 Hearty, P. J., Hollin, J. T., Neumann, A. C., O’Leary, M. J., & McCulloch, M., 2007. Global sea-level fluctuations
810 during the last interglaciation (MIS 5e), *Quaternary Science Reviews*, **26**(17-18), 2090–2112.
- 811 Hirth, G. & Kohlstedt, D., 2003. Rheology of the upper mantle and the mantle wedge: A view from the
812 experimentalists, in *Inside the Subduction Factory*, pp. 83–105, American Geophysical Union.
- 813 Ho, T., Priestley, K., & Debayle, E., 2016. A global horizontal shear velocity model of the upper mantle from
814 multimode love wave measurements, *Geophysical Journal International*, **207**(1), 542–561.
- 815 Hoggard, M. J., Winterbourne, J., Czarnota, K., & White, N., 2017. Oceanic residual depth measurements, the
816 plate cooling model, and global dynamic topography, *Journal of Geophysical Research: Solid Earth*, **122**,
817 2328–2372.
- 818 Hoggard, M. J., Czarnota, K., Richards, F. D., Huston, D. L., Jaques, A. L., & Ghelichkhan, S., 2020. Global
819 distribution of sediment-hosted metals controlled by craton edge stability, *Nature Geoscience*, **13**.
- 820 Huang, P., Wu, P., & Steffen, H., 2019. In search of an ice history that is consistent with composite rheology in
821 glacial isostatic adjustment modelling, *Earth and Planetary Science Letters*, **517**, 26–37.
- 822 Jackson, I. & Faul, U. H., 2010. Grainsize-sensitive viscoelastic relaxation in olivine: Towards a robust

- 823 laboratory-based model for seismological application, *Physics of the Earth and Planetary Interiors*, **183**,
824 151–163.
- 825 Jain, C., Korenaga, J., & ichiro Karato, S., 2019. Global analysis of experimental data on the rheology of olivine
826 aggregates, *Journal of Geophysical Research: Solid Earth*, **124**(1), 310–334.
- 827 Karato, S., 1993. Importance of anelasticity in the interpretation of seismic tomography, *Geophysical Research*
828 *Letters*, **20**(15), 1623–1626.
- 829 Karato, S. & Wu, P., 1993. Rheology of the upper mantle: A synthesis, *Science*, **260**(5109), 771–778.
- 830 Kaufmann, G., Wu, P., & Ivins, E. R., 2005. Lateral viscosity variations beneath antarctica and their implications
831 on regional rebound motions and seismotectonics, *Journal of Geodynamics*, **39**(2), 165–181.
- 832 Kendall, R. A., Mitrovica, J. X., & Milne, G. A., 2005. On post-glacial sea level - II. numerical formulation and
833 comparative results on spherically symmetric models, *Geophysical Journal International*, **161**(3), 679–706.
- 834 Kopp, R. E., Simons, F. J., Mitrovica, J. X., Maloof, A. C., & Oppenheimer, M., 2009. Probabilistic assessment
835 of sea level during the last interglacial stage, *Nature*, **462**(7275), 863–867.
- 836 Kuchar, J., Milne, G., & Latychev, K., 2019. The importance of lateral earth structure for north american glacial
837 isostatic adjustment, *Earth and Planetary Science Letters*, **512**, 236–245.
- 838 Kustowski, B., Ekström, G., & Dziewoński, A. M., 2008. Anisotropic shear-wave velocity structure of the earth's
839 mantle: A global model, *Journal of Geophysical Research*, **113**(B6).
- 840 Lambeck, K., Purcell, A., Funder, S., Kjær, K., Larsen, E., & Möller, P., 2006. Constraints on the late saalian to
841 early middle weichselian ice sheet of eurasia from field data and rebound modelling, *Boreas*, **35**(3), 539–575.
- 842 Lambeck, K., Purcell, A., & Dutton, A., 2012. The anatomy of interglacial sea levels: The relationship between
843 sea levels and ice volumes during the last interglacial, *Earth and Planetary Science Letters*, **315-316**, 4–11.
- 844 Latychev, K., Mitrovica, J. X., Tromp, J., Tamisiea, M. E., Komatitsch, D., & Christara, C. C., 2005. Glacial
845 isostatic adjustment on 3-d earth models: a finite-volume formulation, *Geophysical Journal International*,
846 **161**(2), 421–444.

- 847 Lau, H. C. P. & Holtzman, B. K., 2019. “measures of dissipation in viscoelastic media” extended: Toward
848 continuous characterization across very broad geophysical time scales, *Geophysical Research Letters*, **46**(16),
849 9544–9553.
- 850 Lau, H. C. P., Mitrovica, J. X., Auermann, J., Crawford, O., Al-Attar, D., & Latychev, K., 2016. Inferences of
851 mantle viscosity based on ice age data sets: Radial structure, *Journal of Geophysical Research: Solid Earth*,
852 **121**(10), 6991–7012.
- 853 Lau, H. C. P., Holtzman, B. K., & Havlin, C., 2020. Toward a self-consistent characterization of lithospheric
854 plates using full-spectrum viscoelasticity, *AGU Advances*, **1**(4).
- 855 Li, T., Wu, P., Steffen, H., & Wang, H., 2018. In search of laterally heterogeneous viscosity models of glacial
856 isostatic adjustment with the ICE-6g_c global ice history model, *Geophysical Journal International*, **214**(2),
857 1191–1205.
- 858 McCarthy, C., Takei, Y., & Hiraga, T., 2011. Experimental study of attenuation and dispersion over a broad
859 frequency range: 2. The universal scaling of polycrystalline materials, *Journal of Geophysical Research*,
860 **116**(B09207).
- 861 Mitrovica, J. & Milne, G., 2002. On the origin of late holocene sea-level highstands within equatorial ocean
862 basins, *Quaternary Science Reviews*, **21**(20-22), 2179–2190.
- 863 Mitrovica, J. X. & Milne, G. A., 2003. On post-glacial sea level: I. general theory, *Geophysical Journal
864 International*, **154**(2), 253–267.
- 865 Muhs, D. R., Simmons, K. R., Schumann, R. R., Schweig, E. S., & Rowe, M. P., 2020. Testing glacial isostatic
866 adjustment models of last-interglacial sea level history in the bahamas and bermuda, *Quaternary Science
867 Reviews*, **233**, 106212.
- 868 Nield, G. A., Whitehouse, P. L., van der Wal, W., Blank, B., O'Donnell, J. P., & Stuart, G. W., 2018. The impact
869 of lateral variations in lithospheric thickness on glacial isostatic adjustment in west antarctica, *Geophysical
870 Journal International*, **214**(2), 811–824.
- 871 O'Leary, M. J., Hearty, P. J., Thompson, W. G., Raymo, M. E., Mitrovica, J. X., & Webster, J. M., 2013. Ice
872 sheet collapse following a prolonged period of stable sea level during the last interglacial, *Nature Geoscience*,
873 **6**(9), 796–800.

- 874 Peltier, W. R., Argus, D. F., & Drummond, R., 2015. Space geodesy constrains ice age terminal deglaciation:
875 The global ICE-6g_c (VM5a) model, *Journal of Geophysical Research: Solid Earth*, **120**(1), 450–487.
- 876 Pico, T., 2019. Towards assessing the influence of sediment loading on last interglacial sea level, *Geophysical*
877 *Journal International*, **220**(1), 384–392.
- 878 Pico, T., Creveling, J. R., & Mitrovica, J. X., 2017. Sea-level records from the u.s. mid-atlantic constrain
879 laurentide ice sheet extent during marine isotope stage 3, *Nature Communications*, **8**(1).
- 880 Polyak, V. J., Onac, B. P., Fornós, J. J., Hay, C., Asmerom, Y., Dorale, J. A., Ginés, J., Tuccimei, P., & Ginés,
881 A., 2018. A highly resolved record of relative sea level in the western mediterranean sea during the last
882 interglacial period, *Nature Geoscience*, **11**(11), 860–864.
- 883 Powell, E., Gomez, N., Hay, C., Latychev, K., & Mitrovica, J. X., 2019. Viscous effects in the solid earth
884 response to modern antarctic ice mass flux: Implications for geodetic studies of WAIS stability in a warming
885 world, *Journal of Climate*, **33**(2), 443–459.
- 886 Priestley, K., McKenzie, D., & Ho, T., 2018. A lithosphere–asthenosphere boundary—a global model derived
887 from multimode surface-wave tomography and petrology.
- 888 Ranalli, G., 1995. *Rheology of the Earth*, Springer, London, 2nd edn.
- 889 Raymo, M. E. & Mitrovica, J. X., 2012. Collapse of polar ice sheets during the stage 11 interglacial, *Nature*,
890 **483**(7390), 453–456.
- 891 Raymo, M. E., Mitrovica, J. X., O’Leary, M. J., DeConto, R. M., & Hearty, P. J., 2011. Departures from eustasy
892 in pliocene sea-level records, *Nature Geoscience*, **4**(5), 328–332.
- 893 Richards, F. D., Hoggard, M. J., Cowton, L. R., & White, N. J., 2018. Reassessing the thermal structure of
894 oceanic lithosphere with revised global inventories of basement depths and heat flow measurements, *Journal*
895 *of Geophysical Research: Solid Earth*, **123**, 9136–9161.
- 896 Richards, F. D., Hoggard, M. J., White, N. J., & Ghelichkhan, S., 2020. Quantifying the relationship between
897 short-wavelength dynamic topography and thermomechanical structure of the upper mantle using calibrated
898 parameterization of anelasticity, *Journal of Geophysical Research: Solid Earth*.

- 899 Rohling, E. J., Hibbert, F. D., Williams, F. H., Grant, K. M., Marino, G., Foster, G. L., Hennekam, R., de Lange,
900 G. J., Roberts, A. P., Yu, J., Webster, J. M., & Yokoyama, Y., 2017. Differences between the last two glacial
901 maxima and implications for ice-sheet, $\delta^{18}\text{O}$, and sea-level reconstructions, *Quaternary Science Reviews*,
902 **176**, 1–28.
- 903 Rovere, A., Raymo, M. E., Vacchi, M., Lorscheid, T., Stocchi, P., Gómez-Pujol, L., Harris, D. L., Casella, E.,
904 O'Leary, M. J., & Hearty, P. J., 2016. The analysis of last interglacial (MIS 5e) relative sea-level indicators:
905 Reconstructing sea-level in a warmer world, *Earth-Science Reviews*, **159**, 404–427.
- 906 Rowley, D. B., Forte, A. M., Moucha, R., Mitrovica, J. X., Simmons, N. A., & Grand, S. P., 2013. Dynamic
907 topography change of the eastern united states since 3 million years ago, *Science*, **340**(6140), 1560–1563.
- 908 Sandstrom, M. R., O'Leary, M. J., Barham, M., Cai, Y., Rasbury, E. T., Wooton, K. M., & Raymo, M. E., 2020.
909 Age constraints on surface deformation recorded by fossil shorelines at cape range, western australia, *GSA*
910 *Bulletin*.
- 911 Schaeffer, A. J. & Lebedev, S., 2013. Global shear speed structure of the upper mantle and transition zone,
912 *Geophysical Journal International*, **194**, 417–449.
- 913 Schaeffer, A. J. & Lebedev, S., 2014. Imaging the North American continent using waveform inversion of global
914 and USArray data, *Earth and Planetary Science Letters*, **402**, 26–41.
- 915 Schuberth, B. S. A. & Bunge, H. P., 2009. Tomographic filtering of high-resolution mantle circulation models:
916 Can seismic heterogeneity be explained by temperature alone?, *Geochemistry, Geophysics, Geosystems*,
917 **10**(5).
- 918 Shakun, J. D., Lea, D. W., Lisiecki, L. E., & Raymo, M. E., 2015. An 800-kyr record of global surface ocean
919 $\delta^{18}\text{O}$ and implications for ice volume-temperature coupling, *Earth and Planetary Science Letters*, **426**, 58–68.
- 920 Skrivanek, A., Li, J., & Dutton, A., 2018. Relative sea-level change during the last interglacial as recorded in
921 bahamian fossil reefs, *Quaternary Science Reviews*, **200**, 160–177.
- 922 Steinberger, B., 2016. Topography caused by mantle density variations: Observation-based estimates and models
923 derived from tomography and lithosphere thickness, *Geophysical Journal International*, **205**, 604–621.

- 924 Steinberger, B. & Calderwood, A. R., 2006. Models of large-scale viscous flow in the Earth's mantle with
925 constraints from mineral physics and surface observations, *Geophysical Journal International*, **167**, 1461–
926 1481.
- 927 Stephenson, S. N., White, N. J., Li, T., & Robinson, L. F., 2019. Disentangling interglacial sea level and global
928 dynamic topography: Analysis of madagascar, *Earth and Planetary Science Letters*, **519**, 61–69.
- 929 Stixrude, L. & Lithgow-Bertelloni, C., 2011. Thermodynamics of mantle minerals - II. Phase equilibria,
930 *Geophysical Journal International*, **184**, 1180–1213.
- 931 Sundberg, M. & Cooper, R. F., 2010. A composite viscoelastic model for incorporating grain boundary sliding
932 and transient diffusion creep: Correlating creep and attenuation responses for materials with a fine grain size,
933 *Philosophical Magazine*, **90**(20), 2817–2840.
- 934 Takei, Y., 2017. Effects of partial melting on seismic velocity and attenuation: A new insight from experiments,
935 *Annual Review of Earth and Planetary Sciences*, **45**, 447–470.
- 936 Thomas, A. L., Henderson, G. M., Deschamps, P., Yokoyama, Y., Mason, A. J., Bard, E., Hamelin, B., Durand,
937 N., & Camoin, G., 2009. Penultimate deglacial sea-level timing from uranium/thorium dating of tahitian
938 corals, *Science*, **324**(5931), 1186–1189.
- 939 Turcotte, D. L. & Schubert, G., 2002. *Geodynamics*, Cambridge University Press, Cambridge, 2nd edn.
- 940 van der Wal, W., Wu, P., Wang, H., & Sideris, M. G., 2010. Sea levels and uplift rate from composite rheology
941 in glacial isostatic adjustment modeling, *Journal of Geodynamics*, **50**(1), 38–48.
- 942 van der Wal, W., Barnhoorn, A., Stocchi, P., Gradmann, S., Wu, P., Drury, M., & Vermeersen, B., 2013.
943 Glacial isostatic adjustment model with composite 3-d earth rheology for fennoscandia, *Geophysical Journal*
944 *International*, **194**(1), 61–77.
- 945 van Hinsbergen, D. J., Vissers, R. L., & Spakman, W., 2014. Origin and consequences of western Mediterranean
946 subduction, rollback, and slab segmentation, *Tectonics*, **33**, 393–419.
- 947 Vyverberg, K., Dechnik, B., Dutton, A., Webster, J. M., Zwart, D., & Portell, R. W., 2018. Episodic reef
948 growth in the granitic seychelles during the last interglacial: Implications for polar ice sheet dynamics,
949 *Marine Geology*, **399**, 170–187.

- 950 Waelbroeck, C., Labeyrie, L., Michel, E., Duplessy, J. C., & Mcmanus, J. F., 2002. Sea-level and deep water
951 temperature changes derived from benthic foraminifera isotopic records, *Quaternary Science Reviews*, **21**,
952 295–305.
- 953 Watts, A., Zhong, S., & Hunter, J., 2013. The behavior of the lithosphere on seismic to geologic timescales,
954 *Annual Review of Earth and Planetary Sciences*, **41**(1), 443–468.
- 955 Woodroffe, S. A., Long, A. J., Milne, G. A., Bryant, C. L., & Thomas, A. L., 2015. New constraints on late
956 holocene eustatic sea-level changes from mahé, seychelles, *Quaternary Science Reviews*, **115**, 1–16.
- 957 Wu, P., Wang, H., & Steffen, H., 2012. The role of thermal effect on mantle seismic anomalies under laurentia and
958 fennoscandia from observations of glacial isostatic adjustment, *Geophysical Journal International*, **192**(1),
959 7–17.
- 960 Yamauchi, H. & Takei, Y., 2016. Polycrystal anelasticity at near-solidus temperatures, *Journal of Geophysical*
961 *Research: Solid Earth*, **121**(11), 7790–7820.